A PROGRAMMABLE CURRENT SOURCE FOR MAGNETIC RESONANCE CURRENT DENSITY IMAGING (MRCDI) AT 3 TESLA

A THESIS SUBMITTED TO
THE GRADUATE SCHOOL OF NATURAL AND APPLIED SCIENCES
OF
MIDDLE EAST TECHNICAL UNIVERSITY

BY

CİHAN GÖKSU

IN PARTIAL FULFILLMENT OF THE REQUIREMENTS
FOR
THE DEGREE OF MASTER OF SCIENCE
IN
ELECTRICAL AND ELECTRONICS ENGINEERING

FEBRUARY 2014

Approval of the thesis:

A PROGRAMMABLE CURRENT SOURCE FOR MAGNETIC RESONANCE CURRENT DENSITY IMAGING (MRCDI) AT 3T

submitted by **CİHAN GÖKSU** in partial fulfillment of the requirements for the degree of **Master of Science in Electrical and Electronics Engineering Department, Middle East Technical University** by,

Prof. Dr. Canan Özgen
Dean, Graduate School of **Natural and Applied Sciences**

Prof. Dr. Gönül Turhan Sayan
Head of Department, **Electrical and Electronics Engineering**

Prof. Dr. Murat Eyüboğlu
Supervisor, **Electrical and Electronics Engineering Dept., METU**

Examining Committee Members

Prof. Dr. Nevzat G. Gençer
Electrical and Electronics Engineering Dept., METU

Prof. Dr. Murat Eyüboğlu
Electrical and Electronics Engineering Dept., METU

Prof. Dr. Tolga Çiloğlu
Electrical and Electronics Engineering Dept., METU

Assoc. Prof. Dr. Yeşim Serinağaoğlu Doğrusöz
Electrical and Electronics Engineering Dept., METU

Assist. Prof. Dr. Evren Değirmenci
Electrical and Electronics Engineering Dept., Mersin University

Date: 07.02.2014

I hereby declare that all information in this document has been obtained and presented in accordance with academic rules and ethical conduct. I also declare that, as required by these rules and conduct, I have fully cited and referenced all material and results that are not original to this work.

Name, Last name : Cihan Göksu

Signature :

ABSTRACT

A PROGRAMMABLE CURRENT SOURCE FOR MAGNETIC RESONANCE CURRENT DENSITY IMAGING (MRCDI) AT 3 TESLA

Göksu, Cihan
M.Sc., Department of Electrical and Electronics Engineering
Supervisor: Prof. Dr. Murat Eyüboğlu

February 2014, 89 pages

Electrical properties of biological tissues are distinctive between various types of the tissues, and significantly related with the pathological conditions of the tissues. For instance, conductivity images can be used for tumor identification. Besides, current density distribution may provide useful information in research and development of electrical stimulation, electro-surgery, defibrillation, and cardiac pacing devices. Magnetic resonance current density imaging (MRCDI) and magnetic resonance electrical impedance tomography (MREIT) are two imaging modalities based on the current density distribution and the conductivity variation in biological tissues. In this thesis, a four-channel programmable current source to be used in MRCDI and MREIT applications, is designed and implemented. The current source is composed of a microcontroller unit (MCU), a digital to analog converter (DAC), a step-up DC-DC converter, and a voltage to current (V-I) converter with a current steering topology.

Two different MRCDI experiments are performed in this study. In the first experiment, the current density distribution inside a uniform phantom is investigated. In the second experiment, a current steering insulating layer is inserted inside the uniform phantom, and the current density distribution is investigated. In order to check the accuracy of the experiments, the total injected current is compared with the total integrated current, which is calculated from reconstructed current density images. It is concluded that, the experiments are performed with 7.4% error.

Keywords: Magnetic resonance, current density imaging, programmable current source, microcontroller unit, step-up DC-DC converter.

ÖZ

3 TESLA'DA MANYETİK REZONANS AKIM YOĞUNLUĞU GÖRÜNTÜLEME (MRAYG) İÇİN PROGRAMLANABİLİR AKIM KAYNAĞI

Göksu, Cihan
Yüksek Lisans, Elektrik ve Elektronik Mühendisliği Bölümü
Tez Yöneticisi: Prof. Dr. Murat Eyüboğlu

Şubat 2014, 89 sayfa

Biyolojik dokuların elektriksel özellikleri çeşitli doku türleri arasında değişmekte olup, dokuların patolojik durumları ile yakından ilintilidir. Örneğin, iletkenlik görüntüleri tümör tanımlanmasında kullanılabilir. Bunun yanı sıra, akım yoğunluğu dağılımı elektriksel stimülasyon, elektro-cerrahi, defibrilasyon ve kalp pili araçlarının araştırma ve geliştirmesinde yararlı bilgi sağlayabilmektedir. Manyetik rezonans akım yoğunluğu görüntüleme (MRAYG) ve manyetik rezonans elektriksel empedans tomografisi (MREET), biyolojik dokulardaki akım yoğunluğu dağılımı ve iletkenlik değişimi üzerine dayanan iki farklı görüntüleme yöntemidir. Bu tezde, MRAYG ve MREET tekniklerinde kullanılmak üzere dört kanallı programlanabilir akım kaynağı tasarlanmış ve donanımsal olarak gerçeklenmiştir. Akım kaynağı, mikrokontrolör ünitesi, dijital-analog çevirici, yükseltici DA-DA çevirici, ve akım yönlendirme topolojili voltaj-akım çeviricisinden oluşmaktadır.

Bu çalışmada, iki ayrı MRAYG deneyi gerçekleştirilmiştir. Birinci deneyde, tekdüze bir fantom içerisindeki akım yoğunluğu dağılımı araştırılmıştır. İkinci deneyde, tekdüze fantom içerisine akım yönlendirici yalıtkan tabaka yerleştirilmiş, ve akım yoğunluğu dağılımı araştırılmıştır. Deneylerin doğruluğunu kontrol etmek için, toplam enjekte edilen akım ile akım yoğunluğu görüntülerinden hesaplanan toplam akım karşılaştırılmıştır. Deneylerin %7.4 hata ile gerçekleştirildiği sonucuna varılmıştır.

Anahtar Kelimeler: Manyetik rezonans, akım yoğunluğu görüntüleme, programlanabilir akım kaynağı, mikrokontrolör ünitesi, yükseltici DA-DA çevirici.

To My Family,

ACKNOWLEDGEMENTS

I would like to express my gratitude to my supervisor Prof. Dr. Murat Eyüboğlu for his guidance, criticism, favorable advice and suggestions, encouragements and support throughout the entire research.

I would like to thank to Assistant Prof. Dr. Evren Değirmenci, Orkun Tomruk, Balkar Erdoğan, and Hasan Hüseyin Eroğlu for their help and support during the study.

I would like to thank to my lab mates Görkem, Soner, Sasan, Alper, Kerim, Duygu, Ömer, Kemal, Uğur, Ali Reza, Ersin, Ceren, Mohammed Reza, Mir Mehdi, Fourough, Gizem, and the other friends in biomedical engineering group for their encouragement and support.

I would like to thank to Mehdi Sadighi for his patience, encouragement, support and motivation during entire research and especially for endless UMRAM trips and experiments.

I would like to express my appreciation to Meltem Dirim for her understanding, support and standing by me during the study.

This study is supported by METU Research Grant BAP-07-02-2013-101 and Turkish Scientific and Technological Research Council (TUBİTAK) Research Grant 113E301.

Finally, I would like to thank to my family for their continuous love, patience, care, support, understanding and trust. Those feelings have always been keeping me motivated to research during entire study.

TABLE OF CONTENTS

CHAPTERS

LIST OF TABLES

TABLES

LIST OF FIGURES

FIGURES

ABBREVIATIONS

2D	Two-dimensional
ADC	Analog to digital converter
CDI	Current Density Imaging
DAC	Digital to Analog Converter
DSV	Diameter Spherical Volume
FGRE	Fast Gradient Recalled echo
FOV	Field of View
GUI	Graphical User Interface
MCU	Microcontroller Unit
MMB	Mikromedia Board
MRCDI	Magnetic Resonance Current Density Imaging
MREIT	Magnetic Resonance Electrical Impedance Tomography
MRI	Magnetic Resonance Imaging
NMR	Nuclear Magnetic Resonance
PCB	Printed Circuit Board
PPM	Parts Per Million
PWM	Pulse-width Modulation
SQUID	Superconducting Quantum Interference Device
SSR	Solid State Relay
TCES	Trans-cranial Electrical Stimulation
TE	Echo Time
TR	Repetition Time
UMRAM	Ulusal Manyetik Rezonans Araştırma Merkezi
V-I	Voltage to Current

CHAPTER 1

INTRODUCTION

1.1 Magnetic Resonance Current Density Imaging

Electrical properties of biological tissues are distinctive between various types of the tissues, and significantly related with the pathological conditions of the tissues [1], [2]. Therefore, imaging of the electrical properties of the biological tissues may provide significant diagnostic information. For example, the electrical conductivity and the dielectric constant of a tumor tissue are significantly different than those of healthy tissues, so that conductivity images can be used for tumor detection and identification [3]. Also, it is well-known that conductivity variation is related with neural activity. Therefore, conductivity imaging is a possible way for neural mapping [4]. In addition, knowledge of current density distribution is useful for research and development of electrical stimulation, electro-surgery, defibrillation, and cardiac pacing devices [5]–[7]. MRCDI is an imaging modality investigating the current density distribution by using magnetic resonance imaging (MRI). Furthermore, MRCDI is fundamental in development of MREIT, which is a novel imaging modality investigating the conductivity variation. MRCDI can be classified into three groups according to the frequency of externally applied current, which are DC, AC, and RF current density imaging (CDI) [7], [8]. In this thesis, DC CDI by using MRI is studied.

1.2 Development of MRCDI

At the beginning of 1980’s, Holz and Müller investigated the mean velocities of ions in a particular direction in electrolyte solutions by using known nuclear magnetic resonance (NMR) flow measurement techniques, and the effect of an external current on the received NMR signal [9], [10]. Maudsley *et al.* reported the in vitro measurement of magnetic flux density to adjust the magnetic field homogeneity of newly installed main magnets [11]. They used a previously proposed experimental method, which was based on NMR technique of Fourier Imaging. Roth *et al.* proposed a mathematical algorithm to image a two-dimensional current density distribution from its magnetic flux density measurements [12]. The previously proposed algorithm was based on representing the magnetic flux density as the convolution of the current density and a weighting function or Green’s function. A Fourier-based approach was used. In the algorithm, the Fourier transform of the Green’s function was evaluated. With the obtained Green’s function, the current densities were reconstructed by spatial filtering techniques.

The first MRCDI study, which was resulted in the image of a single component of the current density distribution, was performed by Joy *et al.* in 1989 [13]. In the study, they reported a non-invasive direct measurement of the magnetic flux density distribution. The study included both in-vivo and in-vitro experiments for demonstrating the possibility of measuring the magnetic flux density created by externally applied current, which flowed in a volume conductor. For the in-vitro experiment, two concentric cylinders were filled with a saline solution and external current in synchrony with the MRI sequence was applied. The current flow was constrained in only the inner conductor. Standard spin-echo pulse sequence was used. Performing a bipolar current pulse enhanced the phase shifts due to the dynamic magnetic field inhomogeneity, which is corresponding to the phase accumulation of external current in NMR signal. In order to calculate the magnetic flux density component, phase wraps were removed and phase images were scaled, because the corresponding phase images were linearly dependent on gyromagnetic ratio and the pulse-width of the external current. Phase images were calculated for two different cases which were with current and without current. Then the magnetic flux density components due to the external current were calculated. In order to calculate the current density by using Ampere’s law, the directional derivatives of the magnetic flux density components were required. Therefore, the experiment was repeated for different orientations and a single component of current density distribution, which was perpendicular to the selected slice, was calculated. The current was computed as 20µA/mm^2 per pixel with 2.4µA/mm^2 standard deviation. The second experiment was in vitro, and the subject was forearm of a volunteer. The experiment was performed in only one direction. Therefore, the current density distribution could not be calculated. 2mA total current was injected to right anterior forearm from elbow to wrist. The phase images for two different cases, which were with and without external current, were calculated. 70° to -40° phase difference due to the external current was observed in the same region. The results of the study demonstrated the possibility of measurement of current density distribution with 1mm spatial resolution and with a precision of 2.5µA/mm^2 in-vitro. Also, it was shown that detection of magnetic flux density distribution due to 2mA external current was possible in-vivo.

In 1990, Pesikan *et al.* demonstrated the possibility of imaging of two dimensional current density distribution, experimentally [14]. In the experiment, a printed circuit board (PCB) was set in transverse plane, and the current flow was constrained in the surface of the PCB. Z-component of the magnetic flux density produced by the externally applied current was measured. The current density distribution was reconstructed by the Roth’s spatial filtering technique [12]. By this method, the applied current was detected with 10% degradation in the totally applied current. The reconstructed results were compared with the superconducting quantum interference device (SQUID) magnetometer experiment [12]. They reported SQUID method might have detected the current 34000 times less than externally applied current for the same SNR and spatial resolution. They also concluded the current density measurement with higher spatial resolution could have been performed by the MR imaging method under certain circumstances.

Scott *et al.* reported a non-invasive current density measurement technique and performed an experiment with a non-uniform phantom, in 1991 [15]. In the study, the algorithm proposed by Joy *et al.* [13], was used. In [13], only one single component of current density distribution of a uniform cylindrical phantom was imaged. Scott *et al.* extended this study, as calculating all three components of the current density distribution of a non-uniform phantom. The phantom was a cylinder. The non-uniformity was provided by inserting an insulating spherical shell (ping-pong ball) to the center of the phantom. Both the ping-pong ball and the cavity between the ball and the cylinder were filled with a $CuSO_4$ doped saline solution. Similar to the study of Joy *et al.* [13], the standard spin-echo pulse sequence was used with a synchronized bipolar current waveform. All of the three components of the current density distribution could only have been reconstructed by measuring all components of the magnetic flux density and calculating the directional derivatives.
The only component of the magnetic flux density, which was in parallel with the main magnetic field, could have been measured. In order to measure all of the three components of the magnetic flux density, three different experiments were performed. In each experiment, they rotated the phantom, so that the axis of desired magnetic flux density component was aligned with the main magnetic field. Three different slice-selection strategies, which were thin slice, 3D phase encode, and overlapping slice were used. Quantitative comparison of simulations and experimental current density results were done, and the effect of slice selection strategy on resolution, accuracy, and imaging time was discussed.

Sensitivity analysis of MRCDI to random noise and systematic error was performed by Scott *et al.* [16]. In the experiments, they prepared a one-dimensional uniform current phantom. The phantom was a cylindrical tube with two copper electrodes at the both ends, which was inserted in a cylindrical cell. Both the cylindrical tube and the gap between tube and the cylindrical cell were filled with saline solution. Magnetic flux density noise and current density noise were measured for different pixel sizes while without current injection, which ensured the measured noise was only random noise. They concluded that magnetic flux density noise and current density noise were proportional to the square root of pixel size and cubic root of pixel size, respectively. Also the change of current density noise for different echo time (TE) values was observed. They concluded that, choosing pulse-width of the current and TE as 60msec minimized the current density noise, when base resolution was 256, field of view (FOV) was 20cm, and T_2 range was from 40msec to 100msec. In addition, total current for different amplitudes was calculated by both taking surface integral and contour integral. 1.19A/m^2 and 0.15A/m^2 current noise values were calculated for 0.75x0.75x5mm and 1.5x1.5x5mm voxel sizes, respectively. The importance of pixel size in the calculated noise in the reconstructed current density distribution was demonstrated.

In 1997, Sersa *et al.* studied in mapping the spatial distribution of current density in mice tumors [17]. The study was performed to indicate the changes in current density for different electrode geometries, which might have been used in monitoring the effects of electro-chemotherapy. In the study, both in-vivo and in-vitro experiments were performed. In-vivo experiments covered CDI measurement in four T50/80 mammary carcinomas grown subcutaneously on the flanks of nude immunosuppressed mice. In-vitro experiments covered CDI measurement in four SA-1 sarcomas and two B-16 melanomas grown subcutaneously on the flanks of male A/J and CBA mice, respectively. The results of the study indicated the current density distribution through tumors for three different electrode geometry, which were flat, point, and a pair of flat and point electrodes. Also higher current density distribution was reported in the tumor periphery. Beravs *et al.* performed a similar study in bone structures for different magnitudes of current injection [18]. Four fresh chicken femur bone samples, two bone samples which were immersed in 0.7M solution of sodium salt of ethylendiaminetetraacetic acid, two broken bone samples, and four bone samples with different saline solutions were prepared to determine simulating bone fracture and insertion of an insulator during imaging, osteoporosis model, simulating real bone fracture, and the effect of the conductivity of the immersed fluid, respectively. Conventional MR images and current density images of central slice in transverse plane were compared. Similar contrast patterns in both conventional MR images and current density images were observed. They observed current density images had relatively larger noise than the conventional MR images. Feasibility of detection of changed bone structures due to lack of Ca^{+2} ions and increased porosity were demonstrated. Possibility of distinguishing the regions with undisturbed current density and regions with no current due to the insulating object or fracture gap was reported. Also, they concluded conductivity of the solution, in which the bone was immersed, had no effect on the contrast pattern of the reconstructed current density images.

Gamba *et al.* studied the artefacts in current density images caused by the effect of the connection of current carrying cables, in 1997 [19]. They stated the importance of twisting cables to reduce the interference of direct current induced magnetic flux density. In the study, a cylindrical phantom was designed similar to the phantom which was prepared by Joy *et al* [13]. From the reconstructed current density distribution, integrated current and the error was calculated for two different experiments. They concluded the importance of placing conducting wires parallel with the main magnetic field, and rigidly fixed for exact magnetic flux density measurement.

In 1998, Eyüboğlu *et al.* studied imaging current density distribution in non-uniform and uniform phantoms. The experimental study was similar to Joy *et al.'s* and Scott *et al.'s* studies [13], [15]. The lowest current density measured was $2.4\mu A/m^2$ in these studies. As an improvement, Eyüboğlu *et al.* reported the lowest current density measured as $1\ \mu A/m^2$. In addition, the effect of different current levels on k-space data was investigated. The distortion of the acquired signal when applying high current was reported.

Beravs *et al.* worked in MRCDI for imaging the conductivity changes due to chemical processes or reactions, in 1999 [20]. In this study, spatial and temporal distribution changes in ionic concentrations while dissolving of NaCl and $CaCO_3$ were observed. Both NaCl and $CaCO_3$ experiments were performed in Plexiglas cells filled with 0.7% agar-agar gel. Current density images were reconstructed for different time intervals during dissolution process. The ionization in both experiments was demonstrated by current density images. Reconstructed current density images were compared with conventional MRI images. While conventional MRI images could only indicate the change in the size of the crystals, CDI images could also indicate the ionization process as a change of conductivity.

In 1999, Gamba *et al.* studied the detection of changes in current density in tissues of both living and post-mortem piglet heads [21]. Total current was calculated from reconstructed images, by using contour integral. For 60mA current injection, total integrated current was calculated as 47.8mA for both experiments. 12.2mA missing current was supposed to be flowing at the surface of the head through the tissues and could not be measured due to the edge artifacts. Total integrated current was calculated as 62% higher in the brain of living piglet than the brain of post-mortem piglet. Therefore, the difference in conductivity between a death brain tissue and a living brain tissue was demonstrated. Following Gamba *et al.'s* study [21], Joy *et al.* studied in imaging current density distribution and investigating current pathways inside the skull of rabbits during trans-cranial electro-stimulation (TCES) [22]. The study covered three main objectives, which were to estimate the total values of impulse current, identifying different regions in brain by observing the change in current density level, and to follow the current pathways in brain. The experiments were performed in four different anesthetized, paralyzed, artificially ventilated, and post-mortem New Zealand rabbits. The current was injected by five copper electrodes which were placed as one on the forehead, two symmetrically between eyes and ears, and two behind ears. Current density images were reconstructed for both sagittal and bilateral current injection, and the current pathways were calculated from current density vectors. The dependence of current density distribution to the direction of applied current was demonstrated. The reconstructed images and pathways were compared with the simulations. Significantly different experimental and simulation results were acquired. The difference was supposed to be for the existence of extremely heterogeneous and anisotropic structures in the skull, which was neglected in the mathematical models. Also, the difference in current density distribution between the skulls of a rabbit and a human during TCES was demonstrated.

In 2001, Özbek *et al.* studied in measuring the z-component of the magnetic flux density in field strength as low as 0.15T [23]. In this study, the designed phantom was 15x15x2cm rectangular prism. Two experiments were performed. In the first experiment, a uniform phantom is used. In the second experiment, a circular insulator was inserted inside the uniform phantom. The z-component of the magnetic flux density was measured, and possibility of imaging current density distribution in field strength as low as 0.15T was demonstrated.

Demonte *et al.* studied in correction of two CDI artifacts, which were image distortion and image mis-registration, in 2002 [24]. Non-linearity of the gradient fields caused image distortion, and image distortion caused mis-registration. Because the mis-registration violated one of the Maxwell's equation used in CDI, which was called as Gauss's Law for Magnetism, reconstructed CDI images and the current density vectors were wrongly calculated. In the study, the measurement of the distortion in a phantom which consisted of 3D rectangular array of spheres and fixing the mis-calculation of the current density vectors were demonstrated. The corrected images by mapping and interpolation were reported and compared with the distorted ones. In the same year, they performed a similar experiment and the image distortion was demonstrated in the CDI images of a post-mortem pig [25].

In 2003, Oh *et al.* studied in developing a novel algorithm for the elimination of the subject rotation requirement in MRCDI [26]. In the study, only one component of magnetic flux density measurement was used. The proposed algorithm was based on applying Ampere's Law in frequency domain, and using the Gauss's Law for magnetism. Simple acrylic tube phantom was designed and used. The simulation results and experimental results were compared, and similar current density images were reconstructed. Therefore, they verified that the proposed algorithm was a potential algorithm to be used in in-vivo studies.

In the same year, Demonte *et al.* extended their previous studies [24], [25], and reconstructed corrected CDI images and current density vectors [27]. In the study, a similar phantom in [24] was designed and experimented. The corrected maps were obtained and used in the correction of the experiment, in which the subject was a 3kg post-mortem pig. The correction of the distortion due to mis-registration in the current density vectors and reconstructed CDI image was demonstrated.

In 2003, Demonte *et al.* reported the effectiveness of using a fast gradient recalled echo (FGRE) sequence in CDI [28]. In the study, cylindrical and hemi-sphere gel phantoms composed of animal hide gelatin and agar mixture were used. The current density images and current density vectors were reconstructed for both standard spin-echo pulse sequence and FGRE. Almost similar current pathways were obtained. The results indicated that almost same SNR could have been obtained by FGRE with a significantly shorter scan time.

In 2003, Yoon *et al.* reported the reconstructed current density distribution and streamline analysis from the calculated current density vectors for a phantom filled with gel which simulated breast with malignant tumor [29]. They performed two different experiments with different electrode locations (90° and 180° electrode placement) and compared the experiments. They concluded 180° electrode placement could have been used to image even remote regions of the phantom, while 90° electrode placement could have only been used in imaging of only local regions.

The first study in imaging the volume current density inside post-mortem pig torso was performed by Yoon *et al.* [30]–[33]. The current density vectors were calculated for chest wall and heart. Therefore, the studies were milestone in understanding of the current density distribution inside human body during defibrillation. Also, the streamline analysis performed in [30], [31], which supported the relationship between the anisotropic tissue conductivity and the direction of current flow.

In 2004, Demonte *et al.* studied in imaging volume current density inside a pig torso, and investigating the effect of the post-mortem state of the subject on the reconstructed current density vectors and streamline analysis [34]. The comparison of calculated current density vectors and streamline analysis were performed between in-vivo, post-mortem (~15min. after death), and post-mortem (~60min. after death). They reported that all of the experiments resulted in almost same reconstructed current density vectors and streamline data, which demonstrated the post-mortem state of the subject did not change the volume current density.

In 2006, Yan *et al.* extended Demonte *et al.'s* previous studies [24], [27], to correct the reconstructed CDI images and current density vectors [35]. In the previous studies [24], [27], the image distortion due to the non-linearity in the gradient field and the correction of the distortion were demonstrated. In this study, the distortion due to taking phase derivative was investigated. Full correction of two artifacts in CDI images and current density vectors were reported as an improvement to the previous studies [24], [27]. Similar phantom was used in the experiments, and calibration map was extracted for spatial distortion elimination due to the mis-registration. This method eliminated the image distortion due to the non-linearity in the gradient field. In addition, the distortion due to the phase derivative was eliminated by mapping the distorted derivatives to undistorted space which was performed by multiplying Jacobian matrix of the calibration map with the phase derivative components in the distorted space. In the study, a simple cylinder shape phantom was used. Full correction of both of the artifacts was demonstrated with the reconstructed CDI images and calculated current density vectors.

Demonte *et al.* studied in imaging the current density distribution in-vivo and investigation of the relationship between calculated average current density and total injected current, in 2008 [36]. The study was performed on 4-5kg anesthetized piglets. A 3D FGRE sequence was modified and used. The current density images and current density vectors were reconstructed for 20, 30, and 40mA current injection. For each experiment the average current density was calculated. The results demonstrated the linear relationship between average current density and the total injected current as expected. After their previous study [36], Demonte *et al.* investigated the relationship between the calculated average current density and total injected current further [37]. The same experimental subject and the same pulse-sequence were used. The range of the applied current was extended as from 0mA to 45mA. The average current density was calculated for six different amplitudes. The results demonstrated again the linear relationship between the average current density and the total injected current for a small range of current amplitude, as expected. In 2009, Demonte *et al.* extended their previous studies [36], [37], to investigate the relationship between the average current density and total injected current for a wider range of current amplitude [38]. The same experimental subject and the same pulse-sequence were used. The range of the applied current was from 10mA to 110mA. Three different experiments were performed. Each of the experiment was performed with different range of current amplitude. The collected data set was used to compare the relationship between the average current density and total injected current for the different ranges. The study indicated that, around 20-30mA current injection, non-linear relationship was observed. This evidence demonstrated that the electrical properties of the biological tissues had some non-linearity depending on the amplitude of the injected current.

1.3 Development of Current Source for MRCDI&MREIT

In MRCDI, an external current injection to imaging region is required. Precision of amplitude and pulse-width of the external current significantly influences the calculated magnetic flux density and reconstructed CDI images. Also, it is well-known that, noise elimination in the externally applied current increases the SNR of the reconstructed CDI images. Therefore, using a precise current source for MRCDI is necessary.

In 2004, Kim *et al.* designed a PC-controlled current source for MREIT [39]. The current source operated in synchrony with the MRI pulse sequence. In the experiment, a saline phantom was used. Magnetic flux density images were calculated and the effectiveness of the current source was demonstrated.

Goharian *et al.* designed a current source for CDI applications, which was controlled by a microcontroller, in 2005 [40]. The designed current source had a user-friendly graphical user interface (GUI). Amplitude, polarity and duration parameters of output current could have been selected. The current source operated in synchrony with the MRI pulse sequence. In the study, the amplitude of the output current was determined by a DAC which was controlled by the microcontroller. Current driver was consisted of a low impedance bipolar current output stage with a current steering topology.

In 2006, Oh *et al.* extended the previous Kim *et al.'s* study [39], and reported the design of a PC-controlled MREIT current source [41]. The features of the current source were reported as bipolar current injection capability, arbitrary current waveform setting, electrode switching for discharging the stored charge from the previous injection, optical isolation from the PC control system. In the study, systematic phase artifact described in [16], was eliminated by precise timing arrangement of the output current. The magnetic flux density images were calculated and reported for a saline phantom.

In 2010, Kim *et al.* extended the Oh *et al.'s* study [41], and improved the design and implementation of the previous current source [42]. As improvement, magnetic and electrical shielding for elimination of switching noise, MR compatibility, and ground isolation features were added. The efficiency of the current source was demonstrated by comparing the simulation results with the experimental results of a saline phantom.

In 2010, Topal *et al.* designed and implemented a current source for MREIT [43]. In this study, interleaved current pulse was generated by multiplexer, and V-I converter topology which was composed of high voltage OP-AMPs. The efficiency of the current source was demonstrated by performing CDI experiments on a non-uniform phantom.

In 2012, Cantaş designed and implemented a multi-channel current source for MREIT [44]. The study reported known problems in MREIT due to using single channel current source, which were the error in z-component of magnetic flux density, ΔBz, due to the boundary mismatch, and non-uniform current density distribution in the electrodes. The elimination of these problems by using a multi-channel current source was demonstrated.

In 2013, Göksu *et al.* designed and implemented a multi-channel programmable current source for MRCDI and MREIT [2]. The current source was controlled by an MCU, and amplitude, pulse-width, delay times, and frequency could have been arranged. The current driver was a simple V-I converter which was composed of a transistor and a high voltage OP-AMP. Also, the current driver was fed by high voltage produced by a step-up DC-DC converter. Therefore, the current source was capable of higher amplitude current waveform generation than the previously designed and implemented current sources.

In 2013, Eroğlu *et al.* designed and implemented a programmable current source for MREIT [45]. The current source had similar features with [2], however the current driver topology was different. In the study, boost and buck-boost converters were used, so that high amplitude output current could have been generated by current mirrors in the current driver.

1.4 Objectives of the Study

The significance of imaging current density distribution in different biomedical engineering and clinical applications is already mentioned. A non-invasive method for imaging current density distribution is MRCDI. However, MRCDI requires a constant current source which operates in synchrony with MRI pulse sequence. Also, designing the current source as programmable is reasonable, because current injection with a wide-range of amplitudes and pulse-widths influences the SNR of the reconstructed images and calculated current density vectors. In addition, in J-based MREIT algorithms, current injection in different paths is required [46]. Therefore, designing a multi-channel programmable current source makes the data acquisition easier in MREIT experiments. In addition, in the studies which are for simulating the current density distribution during defibrillation, high amplitude current injection is required [38]. Therefore, enforcing the design with power electronics converters and increasing the output current capability of the current source is meaningful.

The scope of this study is to design and implement a programmable current source for MRCDI and MREIT applications which possesses so called features and using this current source in imaging the current density distribution by using 3T MR tomography.

1.5 Outline of the Thesis

In this thesis, the theoretical background of MRCDI is explained in detail in Chapter 2. Also, the detailed explanation of the topology of the designed and implemented current source is given in the same chapter. Used experimental set-up during the experiments of this thesis along with the implementation of the current source is given in Chapter 3. In Chapter 4, the experimental results of MRCDI experiments, and the experimental results of the implemented current source are given. The final conclusion and discussion is given in Chapter 5.

CHAPTER 2

THEORY

2.1 Introduction

In this chapter, the fundamentals of MRCDI, MREIT, and the topology and operating principles of the programmable current source are given. In Section 2.2, MRCDI and MREIT are explained briefly. In Section 2.3, MRCDI is explained in detail and the mathematical background of this imaging modality is given for a spin-echo pulse sequence. Then the methodology of obtaining the current density distribution is explained. In Section 2.4, the hardware and software topology of the programmable current source, which is developed in this study, are given. In this section, the block diagram of the current source structure, DC supply and regulator, MCU, step-up DC-DC converter, DAC, solid state relay (SSR) driver, V-I converter with current steering, and step-up DC-DC converter controller are explained in detail.

2.2 Magnetic Resonance Current Density Imaging and Magnetic Resonance Electrical Impedance Tomography

Electrical properties of biological tissues differ from tissue to tissue, and imaging of these electrical properties gives significant diagnostic information [2]. For instance, the current density distribution inside the biological tissues can be used for the development of stimulation and cardiac pacing devices, since the conductivity information is significantly related with the physiological activity and the pathological condition of the tissue [2], [47]. Therefore, obtaining the current density distribution inside the object and reconstructing conductivity images of objects provide significant diagnostic information. The current density distribution and reconstructed conductivity images can be achieved by using NMR with high resolution [13], [47]. Imaging modality investigating the current density distribution inside the object is defined as MRCDI and imaging modality investigating the conductivity variation inside the object is defined as MREIT.

The block diagram for MRCDI and MREIT is given in Figure 2.1. The algorithm of these two imaging modalities can be explained as follows. First, an externally applied current is injected to the object. This external current flowing inside the object creates an additional magnetic flux density. This additional magnetic flux density is related with the phase of raw MRI data. Secondly, obtained magnitude and phase images are processed. Afterwards, by applying MRCDI and MREIT algorithms to the corresponding images, the current density distribution and conductivity image of the object are reconstructed.

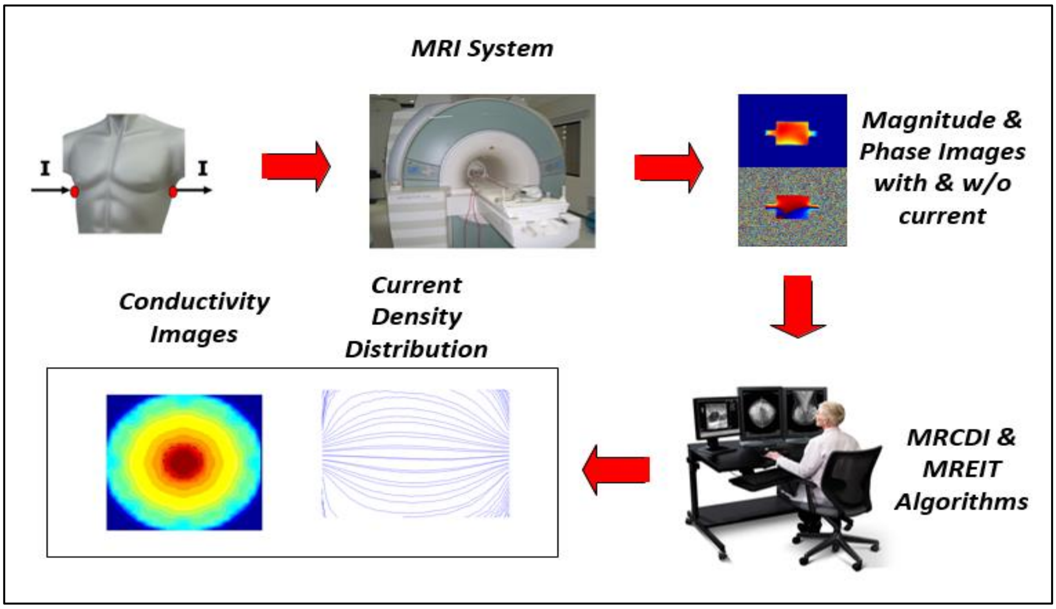

Figure 2.1. Block diagram for MRCDI and MREIT

2.3 Magnetic Resonance Current Density Imaging

Knowledge about the distribution of the externally applied current is essential for many biomedical engineering applications [48]. Therefore CDI is a potential imaging modality which may be used both in scientific and clinical applications. However, CDI has a major drawback that its spatial resolution is not sufficient to be used in clinical purposes. This drawback can be overcome by using the properties of NMR.

In this section, the mathematical background, methodology, and phase unwrapping algorithm for MRCDI are explained in detail.

2.3.1 Mathematical Background of MRCDI

Current density distribution in any material which can be imaged by NMR, is obtained by measuring the magnetic flux density contribution created by an externally applied current [15]. To achieve this, at first acquired NMR signal with a spin-echo pulse sequence is measured. Then, by using the acquired signal, the magnetization density information is expressed for the cases in which external current is applied and not applied. Afterwards, using these magnetization densities the phase contribution of externally applied current is obtained. This phase contribution is linearly dependent with the component of current-induced magnetic flux density in parallel with the main magnetic field and the duration of externally applied current. After obtaining the component of current-induced magnetic flux density in parallel with the main magnetic field, and assuming the components in other directions are negligible, the current density distributions can be reconstructed by using Ampere’s Law [7]. This technique is known as MRCDI.

The standard spin-echo pulse sequence with externally applied current is shown in Figure 2.2.

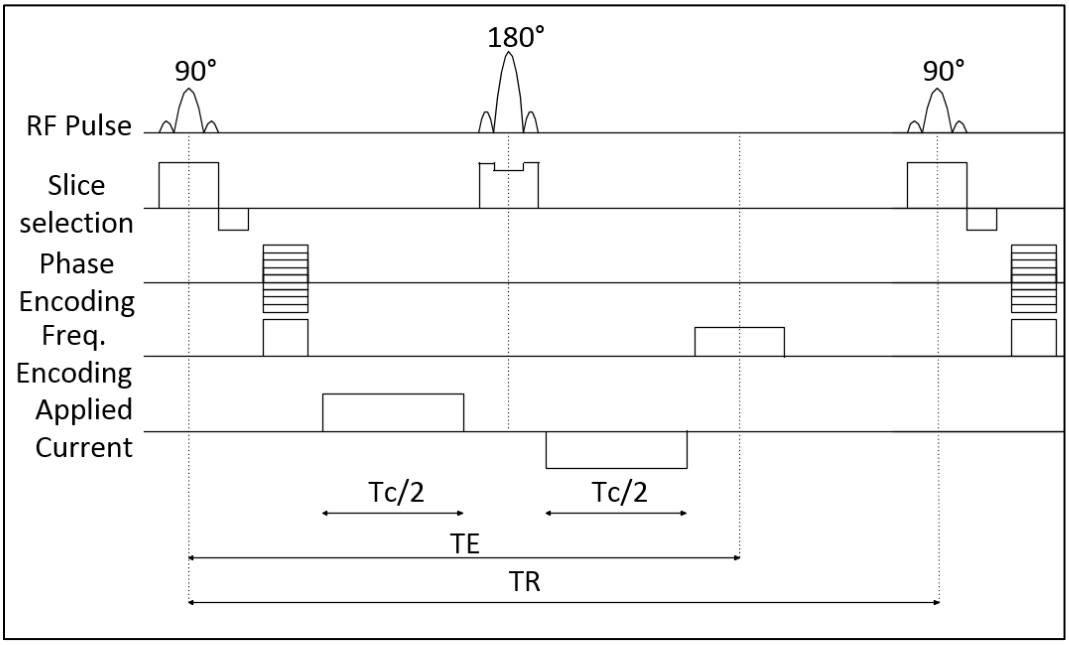

Figure 2.2. Standard spin-echo pulse sequence with externally applied current

Assuming the acquired NMR data is noise-free, the acquired NMR signal with a standard spin-echo pulse sequence is expressed as given in (2.1) [49].

$$S\left(k_x, k_y, t\right) = \iint_{x,y} M(x, y)\, e^{\,j\,(\gamma B t + \emptyset_c + k_x x + k_y y\,)}\, dxdy \tag{2.1}$$

In (2.1), $M(x, y)$ is the continuous real transverse magnetization, γ is the gyromagnetic ratio, B is the magnetic field inhomogeneity, t is the data acquisition time, $\emptyset_c$ is the constant phase contribution due to the instrumentation, k_x and k_y are the spatial frequencies, and *x* and *y* are two-dimensional (2D) space parameters. The spatial frequencies are expressed as given in (2.2) and (2.3),

$$k_x = \gamma\, G_x\, t \tag{2.2}$$

$$k_y = \gamma\, G_y\, t_y \tag{2.3}$$

where G_x , G_y and t_y are frequency encoding gradient strength, phase encoding gradient strength, and pulse-width of the phase encoding gradient, respectively.

The magnetization density, which corresponds to a complex MR image, can be reconstructed by applying Fourier Transform to (2.1) with respect to the spatial frequencies. The reconstructed magnetization density and complex MR image, can be expressed as given in (2.4) and (2.5) [49].

$$M(x,y) = \iint_{k_x,k_y} S\left(k_x, k_y, t\right) e^{-j\,(k_x x + k_y y)}\, dk_x dk_y \tag{2.4}$$

$$M(x,y) = |M(x,y)|\, e^{j\,(\gamma B t + \emptyset_c)} \tag{2.5}$$

When a conductor is exposed to an externally applied current, a constant magnetic flux density is generated. If the conductor is NMR active, and the applied external current is synchronized with the spin-echo pulse sequence, the component of magnetic flux density generated due to the external current in parallel with the main magnetic field of MRI scanner will accumulate a phase to the echo signal. Therefore, in the case of an externally applied current, (2.1) and (2.5) can be modified as given in (2.6) and (2.7) [49],

$$S\left(k_x, k_y, t\right) = \iint_{x,y} M(x,y)\, e^{j\,(\gamma B t + \emptyset_c + \gamma B_j(x,y) T_c + k_x x + k_y y)}\, dxdy \tag{2.6}$$

$$M_j(x,y) = \left|M_j(x,y)\right| e^{j\,(\gamma B t + \gamma B_j(x,y) T_c + \emptyset_c)} \tag{2.7}$$

where, $B_j(x,y)$, T_c, $M_j(x,y)$ are magnetic field intensity due to the externally applied current, pulse-width of externally applied current, and continuous transverse magnetization when external current is applied, respectively.

As the objective is to find the current density distribution, magnetic field intensity due to the externally applied current must be known. The magnetic field intensity due to the externally applied current is linearly related with the phase contribution of the externally applied current to the acquired spin-echo signal. The phase contribution is inferred by dividing (2.7) to (2.5) as given in (2.8).

$$\frac{M_j(x,y)}{M(x,y)} = \frac{|M_j(x,y)|\, e^{\,j\,(\gamma Bt+\gamma B_j(x,y)T_c+\emptyset_c\,)}}{|M(x,y)|\, e^{\,j\,(\gamma Bt+\emptyset_c\,)}} = e^{\,j\,(\gamma B_j(x,y)T_c\,)} \tag{2.8}$$

In (2.8), $\left|M_j(x,y)\right|$ and $|M(x,y)|$ cancel each other and magnetic field inhomogeneities and constant phase term are eliminated. Therefore, phase contribution due to the externally applied current remains. The normalized phase image, $\emptyset_{\mathrm{jn}}$, can be expressed as given in (2.9) [49].

$$\emptyset_{jn}(x,y) = \gamma B_j(x,y)T_c \tag{2.9}$$

Therefore, the magnetic field intensity due to the external current applied can be expressed as given in (2.10).

$$B_j(x,y) = \emptyset_{jn}(x,y)/\gamma T_c \tag{2.10}$$

The gyromagnetic ratio and the pulse-width of the applied current, γ and T_c are constant terms. The gyromagnetic ratio is taken as 26753×10^4 rad.sec^{-1}Tesla^{-1} and the pulse-width of the applied current is determined by the user. From (2.10), current density distributions can be obtained by using Ampere's Law, which can be expressed as given in (2.11).

$$\nabla \times B = \mu_0 J + \mu_0 \epsilon_0 \frac{\partial}{\partial t} E \tag{2.11}$$

With static current flow assumption, the second term is neglected and (2.11) can be re-expressed as given in (2.12).

$$\vec{J} = (\nabla \times \vec{B})/\mu_0 \tag{2.12}$$

In the experiments, the materials with very low magnetic susceptibility are used. Therefore, μ_0, the permeability of free space, is used and taken as $4\pi\times10^{-7}$ Hm^{-1}. When (2.12) is written explicitly, the current density components in all directions can be expressed as given in (2.13), (2.14), (2.15), and (2.16).

$$(\nabla \times \vec{B})/\mu_0 = (1/\mu_0)\begin{bmatrix} \overrightarrow{a_x} & \overrightarrow{a_y} & \overrightarrow{a_z} \\ \frac{\partial}{\partial x} & \frac{\partial}{\partial y} & \frac{\partial}{\partial z} \\ B_x & B_y & B_z \end{bmatrix} \tag{2.13}$$

$$\overrightarrow{J_x} = \frac{1}{\mu_0}\left(\frac{\partial B_z}{\partial y} - \frac{\partial B_y}{\partial z}\right) \tag{2.14}$$

$$\overrightarrow{J_y} = \frac{1}{\mu_0}\left(\frac{\partial B_x}{\partial z} - \frac{\partial B_z}{\partial x}\right) \tag{2.15}$$

$$\overrightarrow{J_z} = \frac{1}{\mu_0}\left(\frac{\partial B_y}{\partial x} - \frac{\partial B_x}{\partial y}\right) \tag{2.16}$$

Therefore, in order to obtain current density distribution in all directions the magnetic flux densities in all directions must be known. In MRCDI, externally applied current creates an additional magnetic flux density in all directions. However, only the parallel component with the main magnetic field is measured. Therefore, this imaging modality requires performing three different experiments for each magnetic flux density measurement. Each experiment is performed by aligning the object’s axes in parallel with the main magnetic field [48].

2.3.2 Methodology of MRCDI

In order to reconstruct the current density distribution inside an object by using MRCDI, the requirement of three different experiments for different orientations is mentioned in the previous section. Three different experiments are shown in Figure 2.3, where the parameters with j subscripts denote the externally applied current cases. The additional magnetic flux density due to the externally applied current can be expressed as given in (2.17). This additional magnetic flux density is linearly dependent on phase of the complex MRI images and has three components. Therefore, three different components of magnetic flux density are obtained by measuring x-oriented, y-oriented, and z-oriented complex MRI images for the cases in which external current is applied and not applied. The methodology of magnetic flux density calculation from complex MRI images is shown in Figure 2.4.

$$B_j(x,y) = B_{jx}\overrightarrow{a_x} + B_{jy}\overrightarrow{a_y} + B_{jz}\overrightarrow{a_z} \tag{2.17}$$

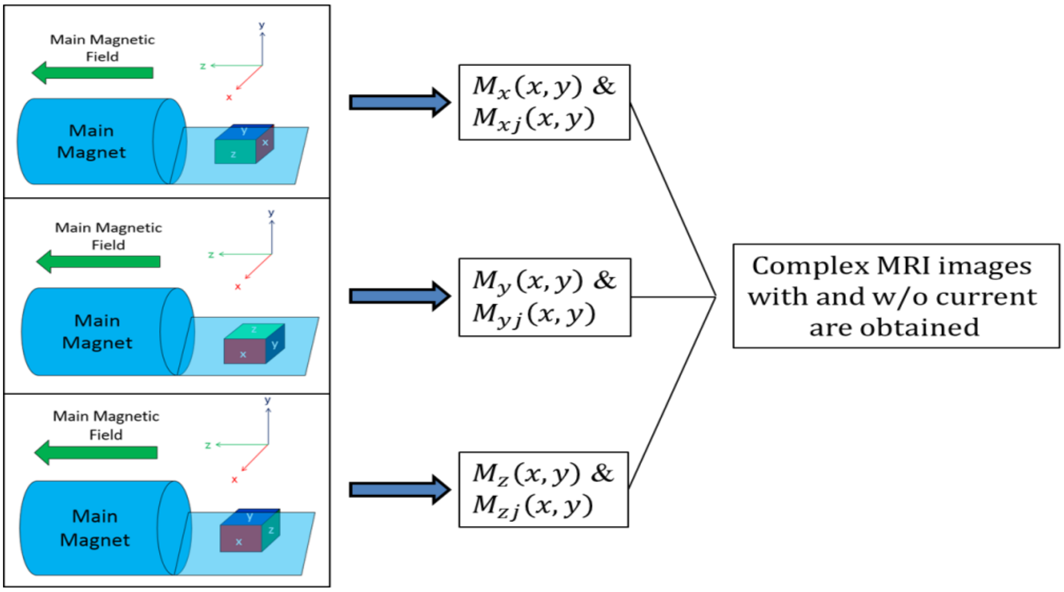

Figure 2.3. Three different experiments to obtain complex MRI images

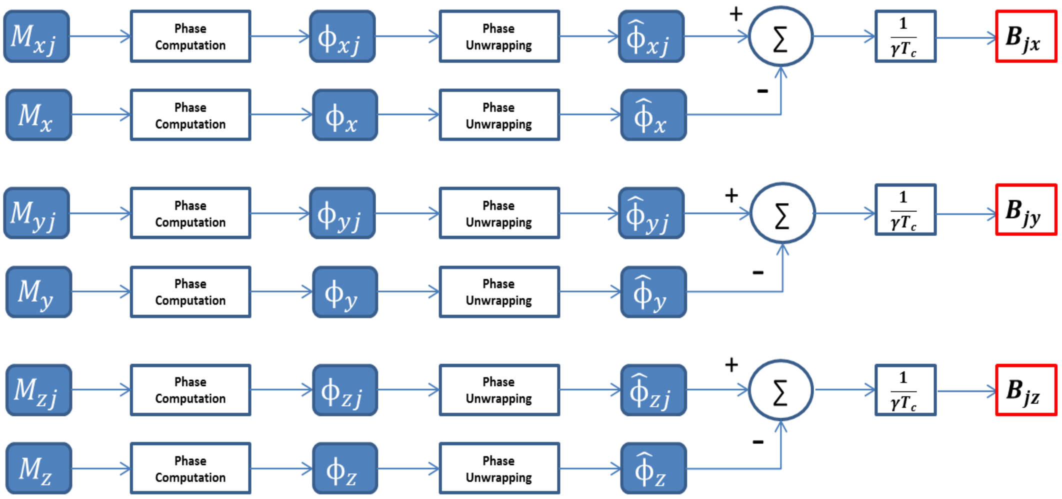

Figure 2.4. Methodology of magnetic flux density calculation from complex MRI images

As shown in Figure 2.4, at first, the phase of each individual complex MRI image for different orientations is extracted. The phase of this image is restricted between [-π, π] interval. Therefore, phase information greater than π or less than –π is wrapped into the phase image. In order to obtain actual phase image, unwrapping of the phase wraps is required. In this study, a model-based method for phase unwrapping is used, which is explained in Section 2.3.3 in detail [50]. The normalized unwrapped phase image due to the externally applied current is obtained by subtracting the unwrapped phase image for the case in which external current is not applied from the unwrapped phase image for the case in which external current is applied. This normalized phase is scaled by $1/(\gamma T_c)$, so that x, y, and z component of magnetic flux density are acquired.

As seen in (2.14) and (2.15), the calculation of J_x and J_y requires $\frac{\partial B_x}{\partial z}, \frac{\partial B_y}{\partial z}, \frac{\partial B_z}{\partial x}$, and $\frac{\partial B_z}{\partial y}$. The methodology for calculation of x and y component of current density distribution is given in Figure 2.5.

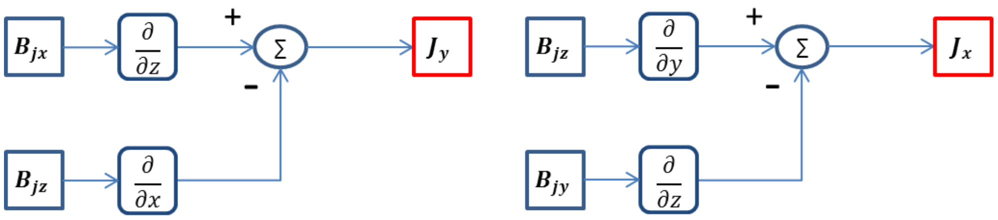

Figure 2.5. Methodology for calculation of x and y component of current density distribution

As z component of the magnetic flux density is measured in transverse plane, x and y derivative of this component is calculated by using image processing techniques. Backward difference is used in the upper and rightmost boundaries of the image. Forward difference is used for the rest of the image. The differentiation in x, y directions and z direction are illustrated in Figure 2.6 and Figure 2.7, respectively. Also, forward and backward difference can be expressed as given in (2.18) and (2.19), respectively [51].

$$\frac{\partial f}{\partial x} = \frac{[f(i,j+1)-f(i,j)]}{\Delta x}\ , \ \frac{\partial f}{\partial y} = \frac{[f(i-1,j)-f(i,j)]}{\Delta y} \qquad (2.18)$$

$$\frac{\partial f}{\partial x} = \frac{[f(i,j)-f(i,j-1)]}{\Delta x}\ , \ \frac{\partial f}{\partial y} = \frac{[f(i,j)-f(i+1,j)]}{\Delta y} \qquad (2.19)$$

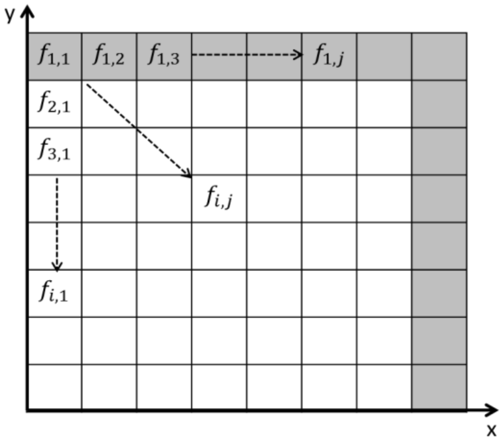

Figure 2.6. Illustration of differentiation in x and y direction of a sample image

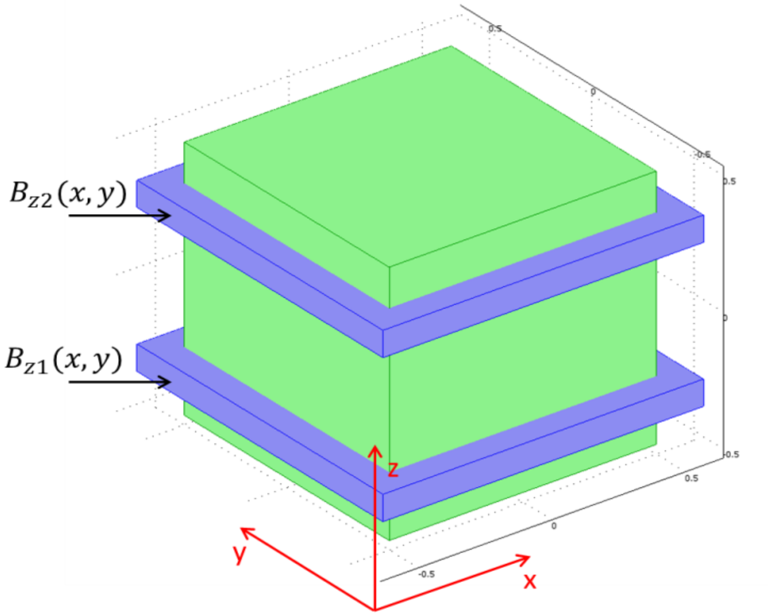

Figure 2.7. Illustration of taking derivative of magnetic flux density in z direction

The current density component calculations require z-derivatives of the magnetic flux density components in x and y directions. For this purpose, performing different experiments are mandatory. Therefore, two consecutive slices are taken for calculating the derivative of both x and y components. The differentiation can be expressed as given in (2.20).

$$\frac{\partial B}{\partial z} = \frac{[B_{z2}(x,y) - B_{z1}(x,y)]}{\Delta z} \tag{2.20}$$

Considering (2.13), x and y components of current density distribution are calculated by using the derivative operations explained in (2.18), (2.19), (2.20).

2.3.3 Phase Unwrapping

Phase images obtained from raw MRI data include phase information restricted between [-π, π] interval. Therefore, phase information greater than π and less than –π is wrapped into this interval. In order to obtain the actual magnetic flux density, wrapped phase information must be eliminated by a phase unwrapping algorithm. The effectiveness of various phase unwrapping algorithms, which are block least squares, adaptive integration, quality guided path following, mask cut, multi grid, and Liang's methods etc. has been compared by J. Strand and T. Taxt [52]. In this study a model-based method for phase unwrapping which has been proposed by Liang is decided to be used [50]. In this section, Liang's method is explained in detail and demonstrated by unwrapping sample images. The corresponding method expresses the phase images as composed of truncated Taylor series and a residual function, which can be expressed as given in (2.21) and (2.22), where $\varphi_{x,y}$, $P_{x,y}, r_{x,y}, C_n(m)$ are phase image, truncated Taylor series polynomial, residual function, and polynomial coefficients, respectively.

$$\varphi_{x,y} = P_{x,y} + r_{x,y} \tag{2.21}$$

$$P_{x,y} = \sum_{n=0}^{N} \sum_{m=0}^{n} C_n(m)\, x^{n-m}\, y^m \tag{2.22}$$

The proposed algorithm is implemented by taking directional derivatives of phase image, calculating the polynomial coefficients, and calculating the residual function. Liang's method proposes to determine the polynomial coefficients by a separate fitting algorithm which can be expressed as given in (2.23) and (2.24).

$$\frac{\partial P_{x,y}}{\partial x} = \sum_{n=1}^{N} \sum_{m=0}^{n-1} (n-m)\, C_n(m)\, x^{n-m-1}\, y^m \tag{2.23}$$

$$\frac{\partial P_{x,y}}{\partial y} = \sum_{n=1}^{N} \sum_{m=1}^{n-1} m\, C_n(m)\, x^{n-m}\, y^{m-1} \tag{2.24}$$

Therefore, $C_n(m)$ can be calculated by solving two weighted least square problems. The corresponding problems can be expressed as given in (2.25) and (2.26), where $w_{x,y}$ are the weighted coefficients.

$$min_{(n-m)\; C_n(m)} \left\{ \sum_x \; \sum_y w_{x,y} \; \left(\frac{\partial \varphi_{x,y}}{\partial x} - \frac{\partial P_{x,y}}{\partial x} \right)^2 \right\} \tag{2.25}$$

$$min_{m\; C_n(m)} \left\{ \sum_x \; \sum_y w_{x,y} \; \left(\frac{\partial \varphi_{x,y}}{\partial y} - \frac{\partial P_{x,y}}{\partial y} \right)^2 \right\} \tag{2.26}$$

Weighted coefficients, $w_{x,y}$, are determined as unity if magnitude of corresponding pixel is greater than a noise threshold and zero otherwise. After obtaining polynomial coefficients, truncated Taylor series polynomial, $P_{x,y}$, is determined. Residual function can be expressed as given in (2.27).

$$r_{x,y} = \; arg\left\{ e^{j[\varphi_{x,y} - P_{x,y}]} \right\} \tag{2.27}$$

Finally, unwrapped phase image is formed with the truncated Taylor series polynomial and residual function. Corresponding unwrapped phase image is expressed in (2.28). Sample wrapped phase images and versions of those unwrapped by using Liang's Algorithm are shown in Figure 2.8.

$$\varphi_{x,y} = \begin{Bmatrix} P_{x,y} + r_{x,y} \,, & if\; w_{x,y} = 1 \\ r_{x,y} \,, & if\; w_{x,y} = 1 \end{Bmatrix} \tag{2.28}$$

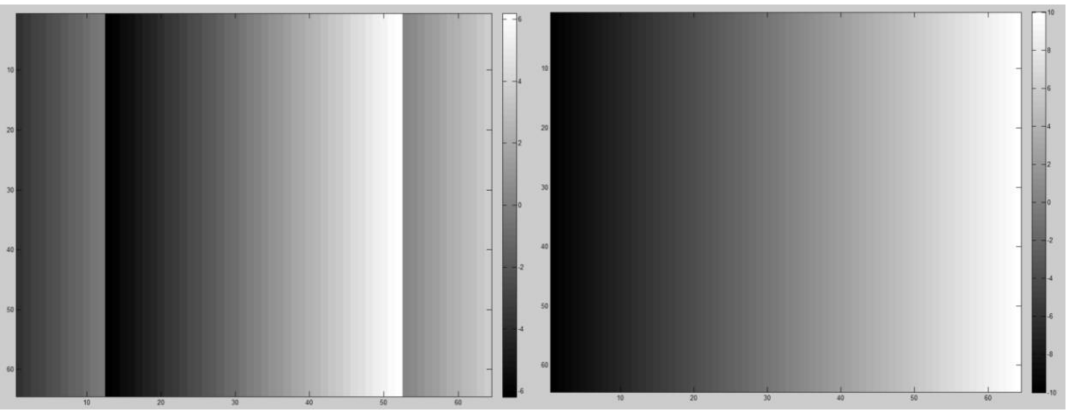

Figure 2.8. Sample wrapped and unwrapped phase images by Liang's algorithm [50]

2.4 Programmable Current Source

As explained in the previous sections, in MRCDI and MREIT, external current injection, which is applied to imaging region, is required. Therefore, design of a constant current source which is in synchrony with the MRI pulse sequence is essential for these imaging modalities. As explained in Section 2.2, the phase accumulation due to the externally applied current is linearly dependent on the pulse-width of the current. In addition, the amplitude of the externally applied current is related with the magnetic flux density contribution of the externally applied current to the obtained MRI signal. Therefore, the exact knowledge of the amplitude and pulse-width of the externally applied current is needed to determine the current density distribution [2]. For this purpose, a programmable current source is designed and implemented.

In this section, block diagram description, power supply and regulator block, step-up DC-DC converter (boost converter), DAC, SSR driver, V-I converter with current steering, step-up DC-DC converter controller, optical transducer, and MCU subsections are explained in detail.

2.4.1 Block Diagram of the Current Source Structure

The overall system of the programmable current source may be divided into different subblocks, which are DAC, SSR driver, optical transducer, V-I converter with current steering, the MCU, the step-up DC-DC converter, and power supply with DC regulator as illustrated in Figure 2.9.

The system is powered by batteries with 24V, -12V. Four main systems are powered by the DC regulator.

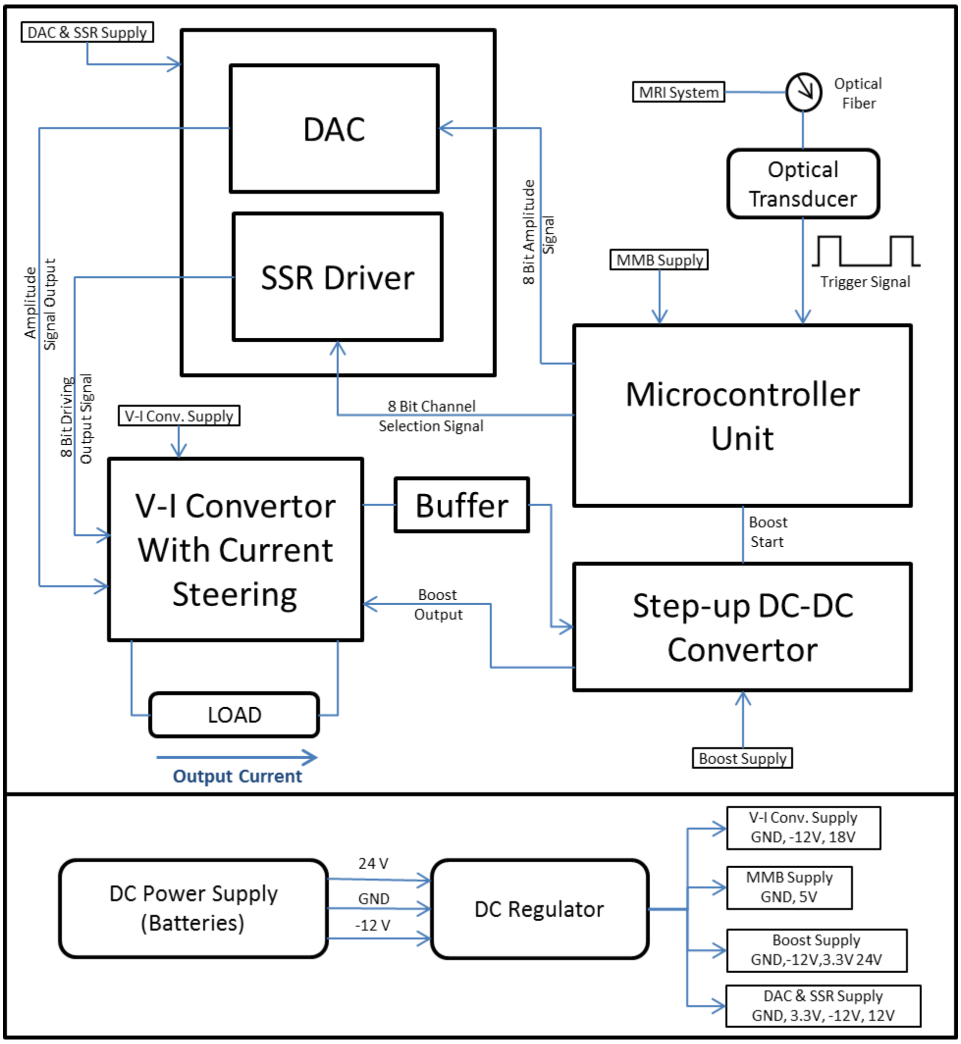

Figure 2.9. The block diagram of the overall system

After the system is ON, GUI in the MCU starts and parameters such as amplitude, frequency, pulse-width and delay time of the output current are selected. According to these output current parameters, the MCU creates two 8-bit digital signals and a start pulse. Desired amplitude of output current is converted to an 8-bit digital signal and transmitted to the DAC unit in parallel. Also, according to the selected channels an 8-bit digital channel selection signal is created and sent to SSR driver for the activation of source and sink channels. At the same time, a start signal is created and sent to the step-up DC-DC converter for producing the required high output voltage.

Upon 8-bit digital amplitude signal, DAC converts an analog amplitude signal. According to 8-bit digital channel selection signal, SSR driver creates and sends 8-bit channel activation signal to V-I converter. At the same time when the step-up DC-DC converter detects the start signal, the step-up DC-DC converter starts to increase the output voltage. For a short period, two dummy channels continuously remain active, in order to detect the minimum required output voltage for desired output current level. When the minimum step-up DC-DC converter output voltage is acquired, the V-I converter sends a feedback to the step-up DC-DC converter by the buffer. As soon as the feedback signal is detected by the step-up DC-DC converter, it stabilizes the output voltage during entire operation. Afterwards, all channels are deactivated by the MCU and trigger signals are waited for activation.

As the system operates in synchrony with the MRI pulse sequence, MRI system sends an optical trigger by fiber optic transmission for each 90° and 180° RF pulses. This optical trigger is converted to a 3.3V electrical trigger signal by an optical transducer and sent to the MCU for creation of current pulses. When each trigger is detected by the MCU, selected source and sink channels are activated for selected durations and current is injected to the load. After 180° pulse trigger is detected, source and sink channels are switched, so that by reversing the current direction a bipolar current pulse is obtained.

2.4.2 DC Supply and DC Regulator

DC supply composed of batteries and the voltage regulation circuits are shown in Figure 2.10. Cooling the regulators for an efficient operation is essential. Heat production of the regulators is highly related with the power dissipation in all individual regulators which is given in (2.29).

$$P_i = \Delta V_i * i_i \tag{2.29}$$

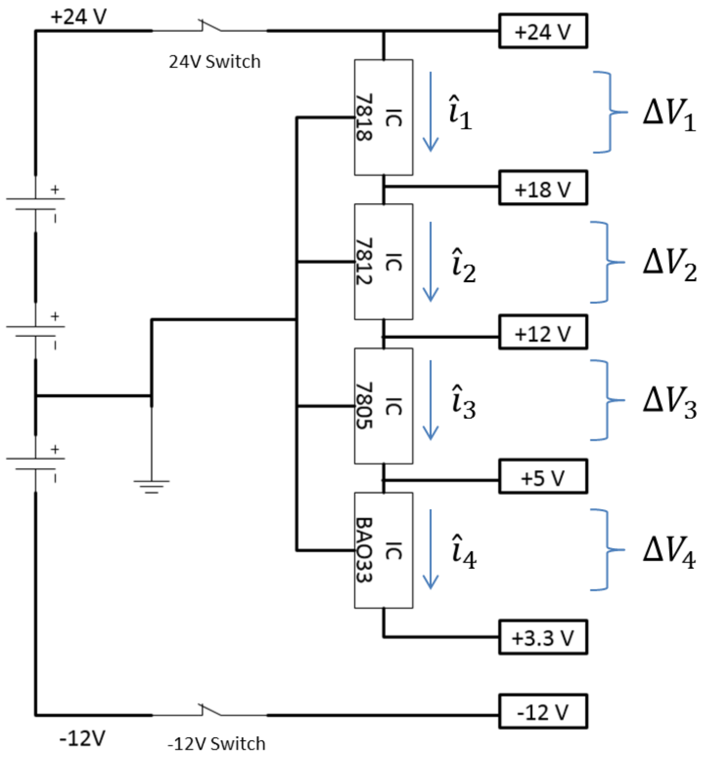

Figure 2.10. The schematic diagram of DC supply and voltage regulation

Power dissipation in each regulator is kept minimal and 18V, 12V, 5V, and 3.3V regulators LM7818, LM7812, LM7805, and BAO33T are used. All of the products have thermal overload current protection, therefore the integrated circuits are cooled by heat-sinks [53].

2.4.3 Microcontroller Unit

Main blocks which are DAC, SSR driver, V-I converter with current steering, and the step-up DC-DC converter are managed by the MCU. In overall system, mikromedia board for dsPIC33 (MMB for dsPIC) is used as the MCU. MMB for dsPIC is a development system which is composed of a TFT 320x240 touch screen display, USB connector, and a pre-programmed UART bootloader. Corresponding compact system is controlled by a 16-bit dsPIC33FJ256GP710A family microcontroller [54].

The MCU is used for detection of electrical trigger signal, creation of 8-bit parallel port output current amplitude data, 8-bit source and sink channel selection data, start signal of the step-up DC-DC converter, and detection of the output voltage of the step-up DC-DC converter. MMB for dsPIC33 also enables a user-friendly GUI. By this way amplitude, frequency, and pulse-width information of the output current pulse is determined. Flow chart of the MCU software is illustrated in Figure 2.11 for only one repetition.

As shown in Figure 2.11, the MCU sets analog and digital ports, stores entered current parameters, and initializes analog to digital converter (ADC) ports, first. When 'RUN' command is given, 8-bit parallel port digital amplitude signal is created according to the stored amplitude, boost start pulse is created, and two arbitrary channels are activated for 20sec. This procedure is for finding the minimum required output voltage. After this 20sec period, the arbitrary channels are deactivated and electrical trigger is started to be checked continuously. When trigger is detected, channels remain as deactivated for forward delay time, which is the time delay after 90° pulse. Then source and sink channels are activated for forward duration time, which is the pulse-width of the (+) cycle of output current. Afterwards, source and sink channels are deactivated and the second trigger signal is started to be waited. When the second trigger comes, source and sink channels are switched. The channels remain as deactivated for inverse delay time, which is the time delay after 180° pulse. Then source and sink channels are activated for inverse duration time, which is the pulse-width of the (-) cycle of output current. Therefore, a bipolar current waveform is obtained for one repetition. The procedure is continued for all repetitions until trigger pulses are ceased.

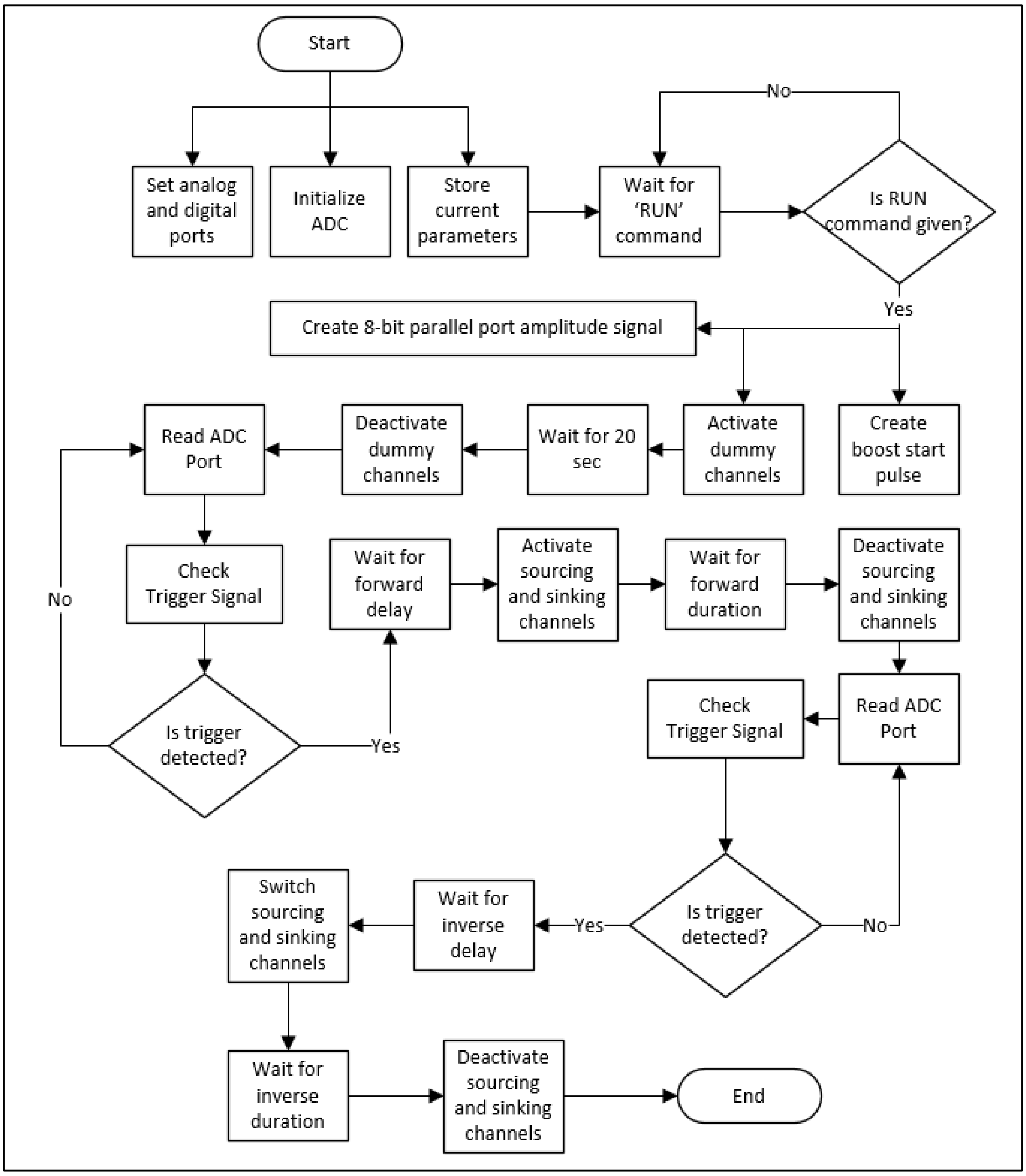

Figure 2.11. Flowchart of the MCU for one repetition

2.4.4 Digital to Analog Converter

V-I converter with current steering topology requires an analog signal, which determines the amplitude of the output current. DAC is used to convert the 8-bit digital amplitude signal, which is sent from the MCU, to the analog amplitude signal. A common 8-bit high speed digital to analog converter, DAC0800 is selected and the typical application circuitry is used [55]. The circuit diagram is shown in Figure 2.12. The MCU sends an 8-bit parallel 0-3.3V state digital data to DAC. DAC0800 divides the reference voltage 3.3V to 256 states and converts 8-bit digital input to analog output signal. Full scale output current of DAC0800 is given in (2.30).

$$I_{FS} = \frac{V_{ref}}{R_{ref}} = \frac{3.3V}{5.1kOhm} = 647uA \tag{2.30}$$

Corresponding full scale current is applicable for DAC0800. In addition, the resolution of the output voltage can be expressed as given in (2.31) [55].

$$\Delta V_{out} = \frac{V_{ref}}{256} = \frac{3.3V}{256} = 12.9mV \tag{2.31}$$

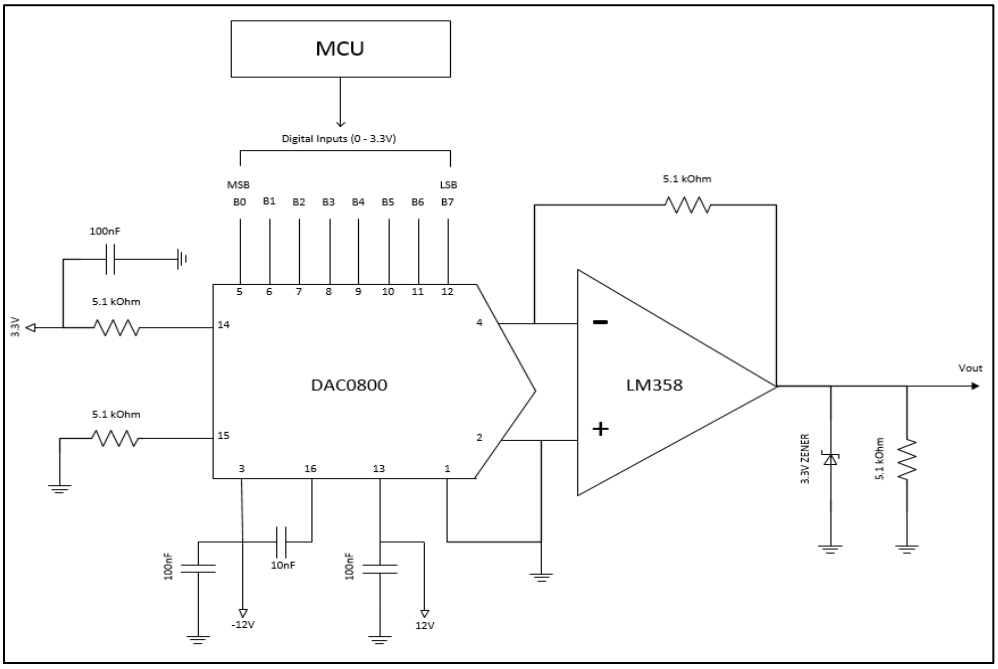

Figure 2.12. The schematic diagram of the typical DAC application circuit

2.4.5 Solid State Relay Driver

Current source topology is composed of four source and sink channels. H-bridge configuration is used in V-I converter topology [40]. Therefore, activation and deactivation of channels require power electronic drivers for high-side switches. In order to eliminate this problem, PVX6012 SSR's are used as switches. By this way, the MCU is electrically isolated from high voltage side and controls switches by photovoltaic relays. However, in order to create an efficient current pulse switches must satisfy high speed operation, low on-state voltage drop, and low off-state leakage current in this topology. For this reason, control current of SSR is significant. The highest speed response is satisfied when control current is at maximum, $I_{cont} = 25mA$ [56]. To satisfy the corresponding control current and drive SSR properly, SSR driver is designed as shown in Figure 2.13. On-state voltage drop of the photodiode is 1.2V so that driving current of SSR is set to 19.8mA as given in (2.32).

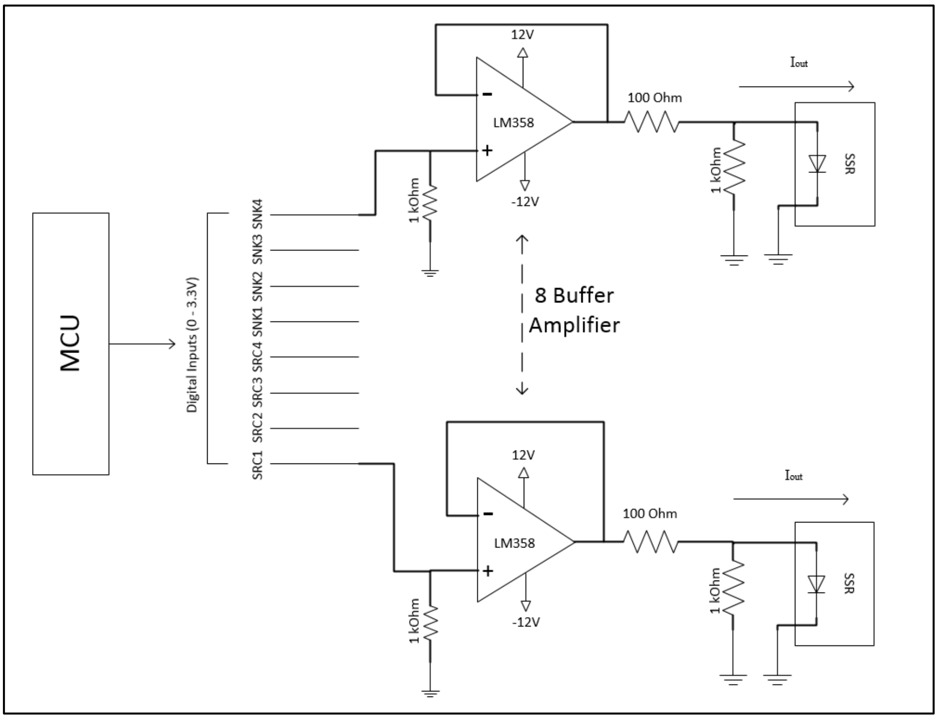

Figure 2.13. The schematic diagram of SSR driver circuit

$$I_{out} = \frac{3.3V - 1.2V}{100Ohm} - \frac{1.2V}{1kOhm} = 19.8mA \qquad (2.32)$$

As shown in Figure 2.13, at first the MCU creates 0-3.3V channel selection pulses. Created pulses are isolated and transmitted by separate buffers. As op-amps operate in linear region, 3.3V output voltages drive SSRs with 19.8mA control current when SSRs are active.

2.4.6 Step-up DC-DC Converter

A step-up DC-DC converter is a power electronic converter used for creating greater output voltages from lower input voltages. The main idea of the step-up DC-DC converter is the property of which inductor resists to changes in current. The topology is basically composed of a switch transistor and two energy storage elements, which are an inductor and a high voltage capacitor. The schematic of the step-up DC-DC converter is shown in Figure 2.14 [57]–[60].

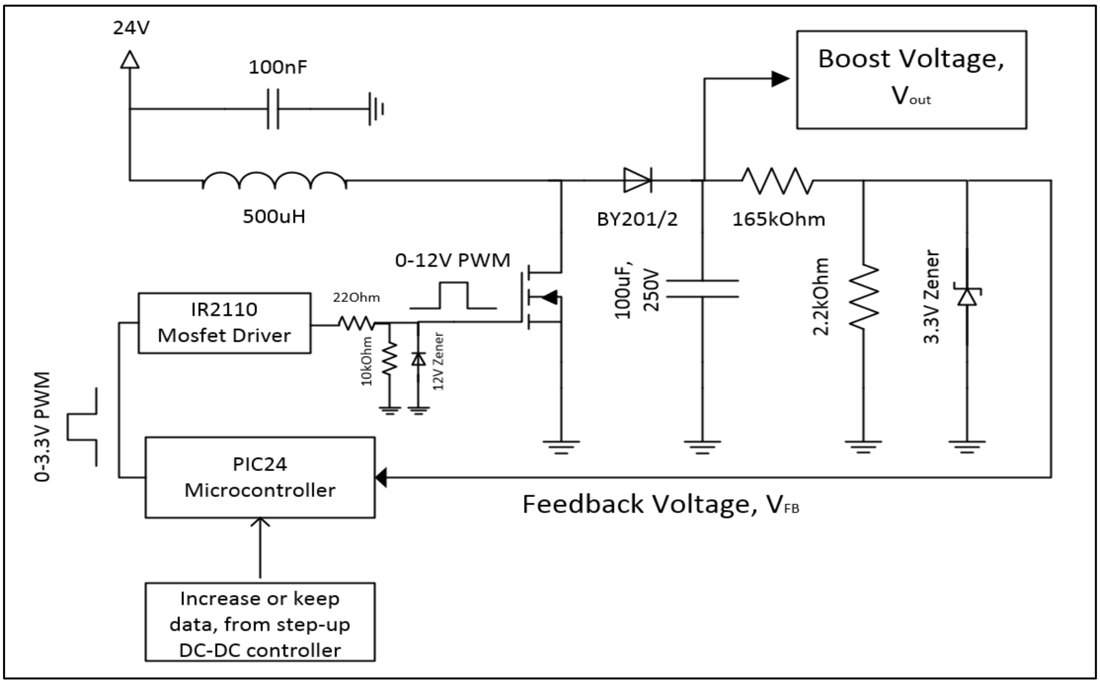

Figure 2.14. The schematic diagram of the step-up DC-DC converter

In continuous-conduction mode, $i_L(t) > 0$, the voltage waveform of the inductor is shown in Figure 2.15. Therefore, the output voltage of the step-up DC-DC converter is illustrated with the switching duty cycle. The overall gain of the system is expressed in (2.33), where D is the switching duty cycle [59].

$$\frac{V_{out}}{V_{in}} = \frac{1}{1-D} \tag{2.33}$$

In this topology, output voltage is stabilized with a hysteresis control feedback mechanism. Output voltage is divided into 0-3.3V interval and sent to a PIC24F04KA200 family microcontroller. Microcontroller converts the analog signal to digital and arranges the duty cycle according to the required output voltage [2], [45], [61]. This is determined by the digital information coming from the step-up DC-DC convertor controller. Step-up DC-DC converter requires high voltage and high-speed power MOSFET drivers. In this topology, IR2110 is used [62]. Corresponding pulse-width modulation (PWM) signal is sent to IR2110 MOSFET driver. IR2110 converts the 0-3.3V PWM to a 0-12V PWM signal. Obtained 0-12V PWM driving signal is stabilized with a voltage driver and applied to gate of the power MOSFET [63]. Therefore, output voltage of the step-up DC-DC converter is stabilized in a desired level.

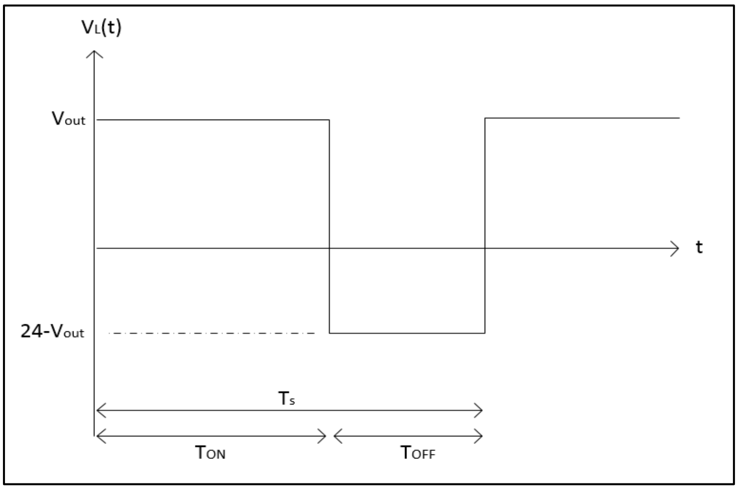

Figure 2.15. The voltage waveform of the inductor in continuous-conduction mode

2.4.7 Step-up DC-DC Converter Controller

A step-up DC-DC converter is a high voltage and high current power electronic converter. The parasitic elements due to losses in capacitor, inductor, diode, and power MOSFET, cause output ripple voltage, switching noise, and negative transient voltage in low side [58], [64]. As the current source is programmable, low current injection does not require high step-up DC-DC converter output voltages. Therefore, arranging the step-up DC-DC converter output voltage according to the desired output current parameters independent of load is necessary. In order to increase the efficiency of the step-up DC-DC converter, decrease the ripple voltage and switching noise, and protect other vulnerable units, the step-up DC-DC converter controller software is designed. The flowchart of the step-up DC-DC converter controller is shown in Figure 2.16.

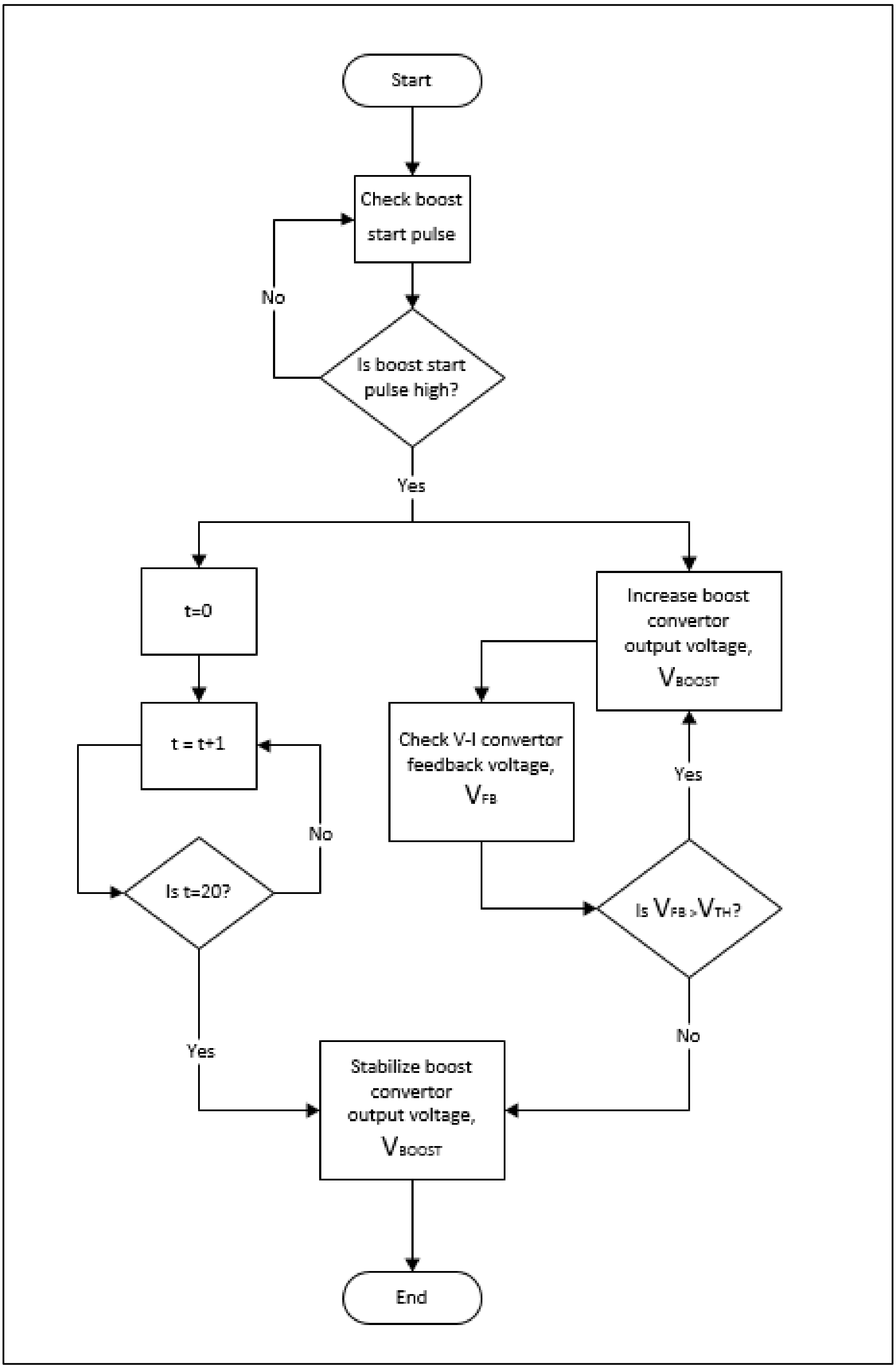

Figure 2.16. The flowchart of the step-up DC-DC controller

As shown in Figure 2.16, after the MCU is initialized and output current parameters are entered, the MCU sends a boost start pulse. Boost start pulse is detected by the PIC24 family microcontroller in the step-up DC-DC controller. During the first 20sec time interval step-up DC-DC converter tries to fix the output voltage to the minimal required voltage for desired current injection. Timer counts for 20sec and stabilizes final high voltage, if the output voltage is not stabilized earlier. During this period, output of the step-up DC-DC converter is increased continuously. To detect the minimum required output voltage, the operating state of the op-amp used in V-I converter is investigated. For this reason, a threshold voltage close to positive saturation voltage of the op-amp is selected. As long as output is not sufficient, V-I converter feedback voltage is equal to (+) SAT voltage of the op-amp used in V-I converter. When output becomes sufficient to inject the desired output current, V-I converter feedback voltage starts to be less than the threshold voltage, which means op-amp used in V-I converter switches its operation to linear region. Afterwards, the minimal output voltage is acquired and stabilized.

2.4.8 V-I Converter with Current Steering

V-I converter with current steering topology is divided into two different parts, which are current steering and V-I converter parts. SSR driver creates an 8-bit driving signal to 8 different channels according to the signals created in the MCU depending on the desired output current parameters. Corresponding driving signals activate and deactivate SSRs, so that source and sink channels are selected. In this study, four channels topology is used. Also, multiple channels activation and deactivation is possible by controlling the driving signals by the MCU. Corresponding current steering topology is shown in Figure 2.17. The second part is the V-I converter part. V-I converter is composed of a high voltage and high current capability op-amp, a power MOSFET, and a current sensing resistor. Used components are OPA452TA, IRF740, and a wire-wound resistor, respectively [65], [66]. The schematic diagram of the V-I converter is shown in Figure 2.17 [67].

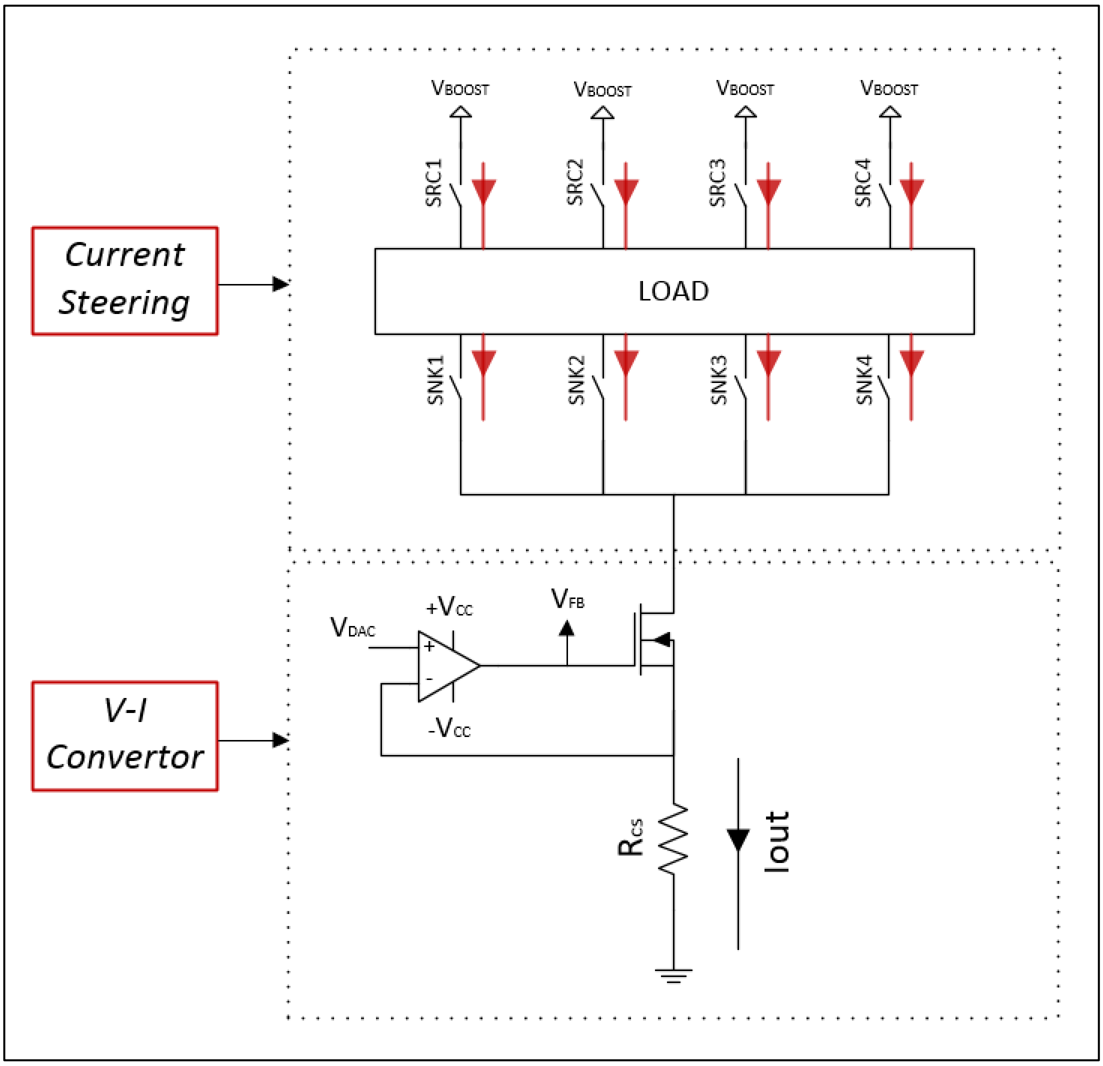

Figure 2.17. The schematic diagram of the V-I converter with current steering topology

The analog signal which is created in DAC determines the amplitude of the output current. Considering full-scale current injection (after step-up DC-DC converter sets the output voltage), op-amp operates in linear region. Therefore (+) and (-) input voltages are both equal to V_{DAC} . Assuming the input impedance of an op-amp is infinite and gate current of a power MOSFET is zero, entire output current is forced to be injected to load connected in the current steering part. Corresponding output current is expressed in (2.34) [67].

$$I_{out} = \frac{V_{DAC}}{R_{CS}} \quad (2.34)$$

The output resistance of the current driver is an important constraint. The values of r_0 and g_m are calculated for I_D=20mA, as the MRCDI experiments are performed for 20mA current injection. The calculated values of r_0 and g_m values of used MOSFET are given in (2.35) and (2.36). The calculated output resistance of the current driver is given in (2.37).

$$g_m = \sqrt{2K_n I_D} = 0.335\ S \quad (2.35)$$

$$r_0 = \frac{1}{\lambda I_D} \cong 53\ k\Omega \quad (2.36)$$

$$R_{out} = R_{CS} + r_0(1 + g_m R_{CS}) \cong 320\ k\Omega \quad (2.37)$$

As mentioned in the step-up DC-DC converter controller, step-up DC-DC converter takes a feedback voltage from V-I converter which informs the op-amp’s operating region. Corresponding feedback voltage is sent to step-up DC-DC converter by a buffer amplifier after feedback voltage is divided into 0-3.3V state. The schematic diagram of the buffer is shown in Figure 2.18.

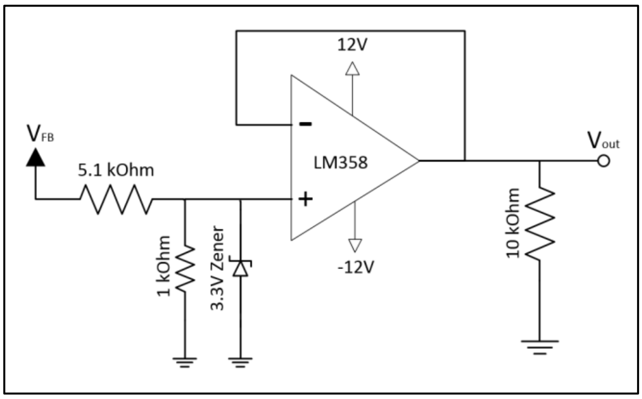

Figure 2.18. The schematic diagram of the buffer

2.4.9 Optical Triggering System

In MRCDI, it is mentioned that in order to accumulate a phase contribution into the MRI signal, externally injected current must be applied in synchrony with the MRI pulse sequence. Therefore, 90° and 180° RF signals must be detected. An optical trigger signal with 1msec duration is sent from the MRI system for each 90° and 180° RF pulses. Corresponding sequence and the timing diagram of the current is shown in Figure 2.19, where Δt_1, Δt_2, Δt_3, and Δt_4 are forward delay, forward duration, inverse delay, and inverse duration respectively. Obtained optical trigger signal is converted to a 0-3.3V electrical signal and sent to the MCU. An ADC port in the MCU continuously checks the trigger port. Therefore, the MCU activates the source and sink channels properly after detecting the electrical trigger signal.

Schematic of the conversion of optical trigger signal to 0-3.3V electrical signal is shown in Figure 2.20.

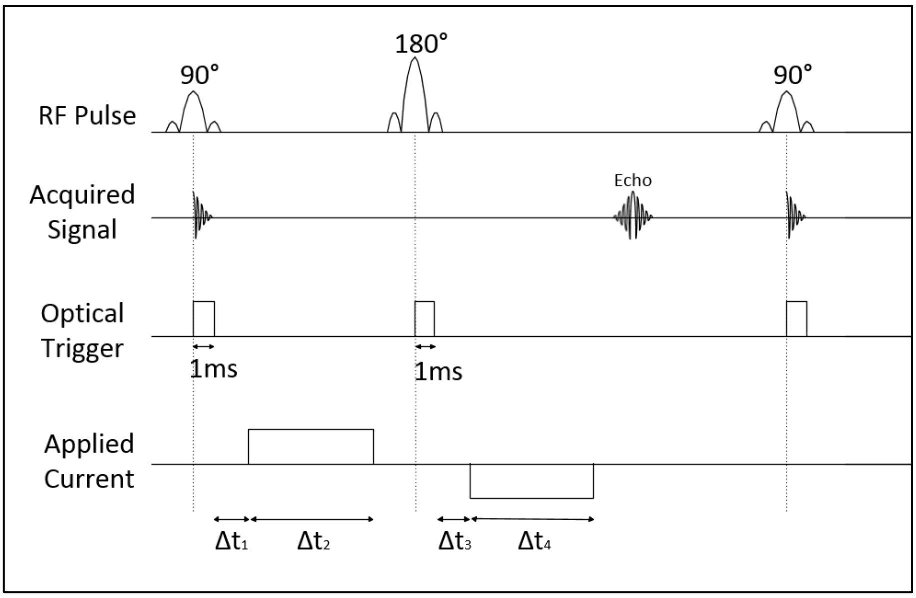

Figure 2.19. The timing diagram of applied current

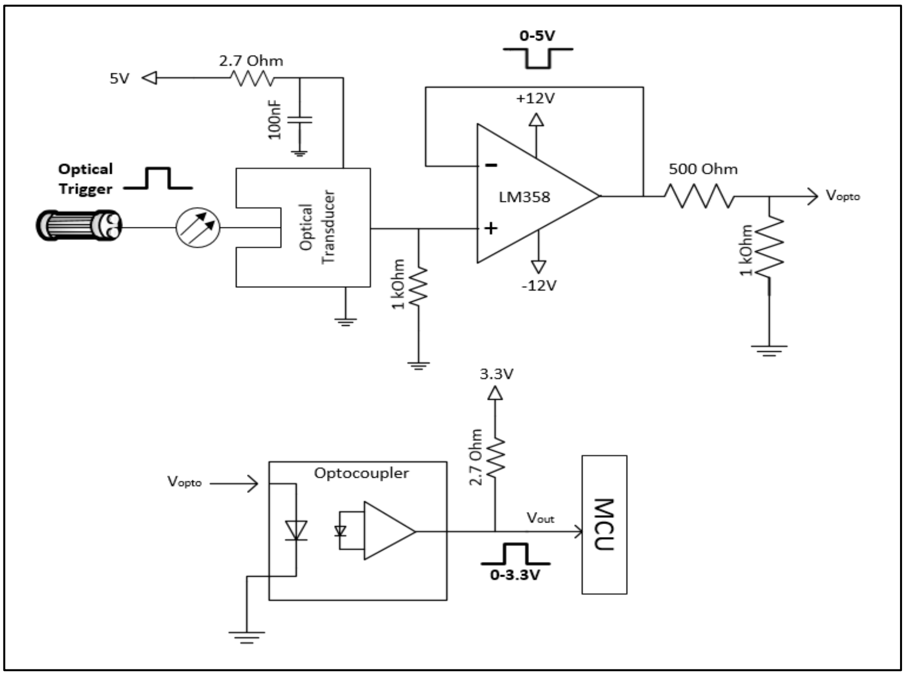

Figure 2.20. The schematic diagram of the conversion of optical trigger signal to electrical signal

Two different 1ms optical trigger pulses are sent to optical transducer by fiber-optic transmission simultaneously with 90° and 180° RF pulses. As optical transducer, HFBR-2528Z receiver is used and it converts optical signal to 0-5V inverted electrical trigger signal [68]. To protect the stability of the MCU operation, this signal is transmitted via a buffer with a pull-down resistor connected to positive terminal of op-amp. Then the inverted trigger signal is converted to non-inverted electrical triggering signal in 0-3.3V state with an opto-coupler, FOD260L. Therefore, output sink current is minimized and time accuracy of the triggering signal is protected [69]. By this way the MCU is protected from any leakage current, and proper detection of trigger signal by ADC port in the MCU is satisfied.

CHAPTER 3

EXPERIMENTAL SET-UP

3.1 Introduction

In this chapter, MRI system which is used in this study and the implemented programmable current source are explained. In Section 3.2, features of the MRI system are mentioned briefly. In Section 3.3, MRI pulse-sequence is explained in detail. In Section 3.4, implementation of the programmable current source is demonstrated. In Section 3.5, two different phantoms which are designed for MRCDI experiments are explained in detail.

3.2 MRI System

In this study, SIEMENS MAGNETOM TRIO^{TM} MRI System at Ulusal Manyetik Rezonans Araştırma Merkezi (UMRAM) is used. Bore diameter of the magnet is 60cm and generated field strength is 3T. Main magnetic field homogeneity is typically 0.1ppm (parts per million) at 40cm DSV (diameter spherical volume). Gradient strength is with standard TQ-Engine 45mT/m at a slew rate of 200T/m/s. The gradients satisfy a FOV as large as 50cm. In the experiments body coil of the MRI system is used. Photographs of the main magnet and console of the MRI system are shown in Figure 3.1 and Figure 3.2.

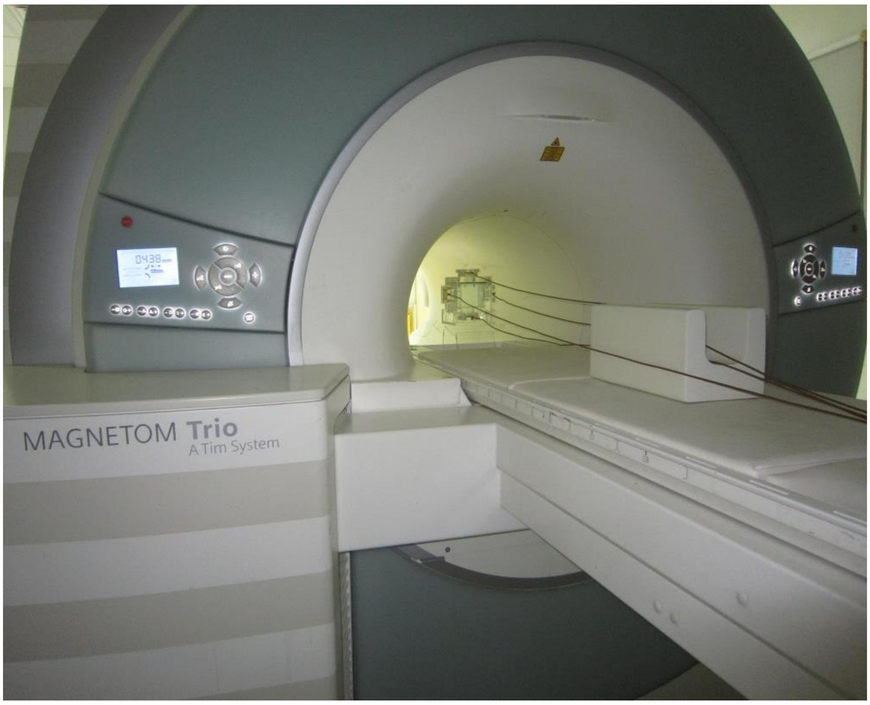

Figure 3.1. Main magnet of the UMRAM MRI system

Figure 3.2. Console of the MRI system

3.3 MRI Pulse Sequence

In this study, a standard spin-echo pulse sequence with a bipolar current pulse is used. The pulse sequence is shown in Figure 2.2. Timing diagram of the bipolar current pulse is shown in Figure 2.19. The synchrony between MRI pulse sequence and the current pulse is satisfied by an optical triggering system. First, the pulse sequence is designed by using pulse-sequence generation program of SIEMENS called as IDEA. In IDEA, user can define all timing parameters such as repetition time (TR), TE etc. In addition, the MRI system has an external optical output port. The optical signal sent to the external port is also managed by the IDEA software program [70]. Therefore, by arranging the timing of optical trigger signal in synchrony with the 90° and 180° RF pulses two different optical trigger signals are generated. These two different optical pulses are converted to 0-3.3V electrical signals, so that the bipolar current pulse is applied in synchrony with the MRI pulse sequence by detection of the electrical signals. Implemented optical triggering system is shown in Figure 3.3.

According to Scott's study for sensitivity analysis of MRCDI [16], the TR and the TE are selected as 250msec and 60msec, respectively for the best SNR. As explained in Chapter 2, the pulse-width of the externally applied current is significantly related with the accumulated phase in the received MRI signal. Therefore, maximizing the pulse-width of the current is an important aspect. Also, the current pulse is applied after the 90° and 180° RF pulses, which eliminates the geometric distortions in the phase image [16]. Therefore, Δt_1, Δt_2, Δt_3, and Δt_4 values, which are shown in Figure 2.19, are selected as 5msec, 20msec, 5msec, and 20msec, respectively. Number of samples of the echo signal and number of phase encodings are selected as 64. Therefore, the base resolution is 64. Also, it is well-known that increasing pixel size and slice thickness gives better SNR [16]. Therefore, the FOV and slice thickness are selected as 128x128mm and 5mm which determines the voxel size as 2x2x5mm.

Figure 3.3. The implemented optical triggering system

3.4 Programmable Current Source

The current source designed in this study is composed of four different hardware blocks, which are the DC regulator, the DAC and SSR driver, the step-up DC-DC converter and the V-I converter with current steering, and the MCU. The photographs of the MCU, the DC regulator, the DAC and SSR driver, and the step-up DC-DC converter and the V-I converter with current steering circuitries are shown in Figure 3.4.

In the MCU a GUI is designed. By the GUI, the output current parameters can easily be selected by the user and entered. The designed GUI is shown in Figure 3.5. The photograph of the implemented current source is shown in Figure 3.6.

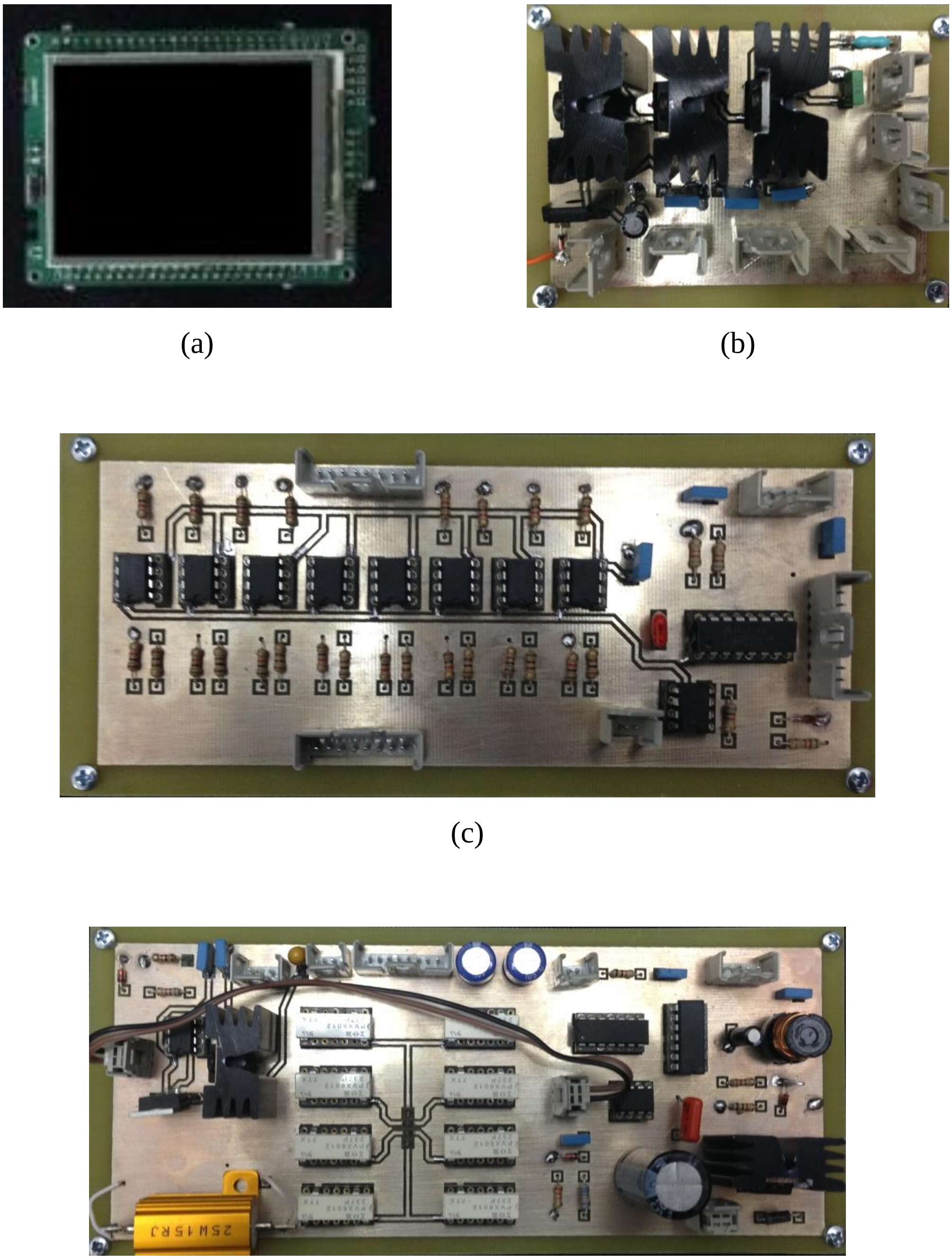

(a) (b)

(c)

(d)

Figure 3.4. Photographs of MCU and implemented circuitries: (a) The MCU, (b) The DC regulator, (c) The DAC and the SSR driver, (d) The step-up DC-DC converter and the V-I converter with current steering

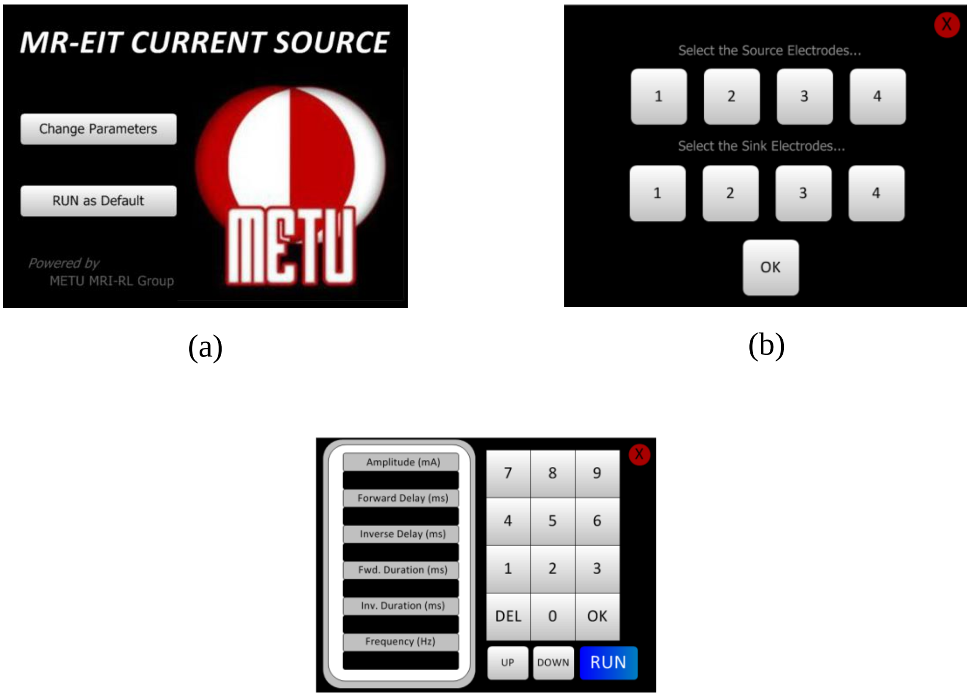

(a)

(b)

(c)

Figure 3.5. Designed GUI layers: (a) Layer 1, (b) Layer 2, (c) Layer 3

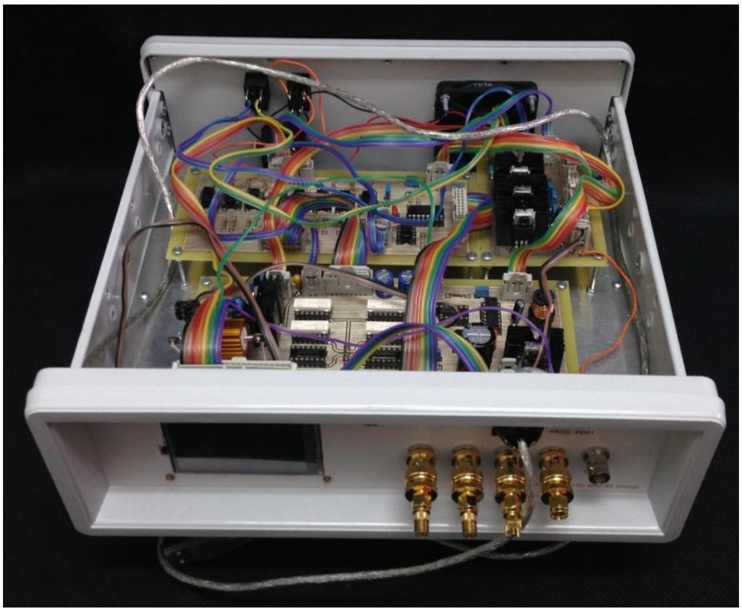

Figure 3.6. Photograph of the implemented current source

3.5 Designed Phantoms for MRCDI Experiments

In this study, two different phantoms are designed and manufactured. First one is the 2D uniform phantom and the second one is the same phantom with current steering insulator object. As the phantoms are placed and rotated inside the main magnet during the experiments, a symmetrical structure is preferred in order to make the rotations of the phantoms easier. One of the side walls of the phantom structure is mounted by using screws. Therefore, different layers can be integrated to the phantoms and different subdomain solutions can be used. Recessed electrodes are used in the design of the phantoms. By this way, the signal loss in the imaging region is eliminated. Also, any non-uniformity in the injected current near the electrodes is kept out of the imaging region. Thin stripped copper electrodes are preferred, to minimize the signal loss in the areas near the electrodes. Because matching all of the magnetic flux density images is required, a phantom holder is manufactured. Therefore, the phantoms are vertically fixed in a position and ease to be rotated. The phantoms and the holder must be manufactured from a nonmagnetic material, so that Plexiglas material is preferred. The technical drawings of the designed phantoms with current simulations are shown in Figure 3.7 and Figure **3.8**.

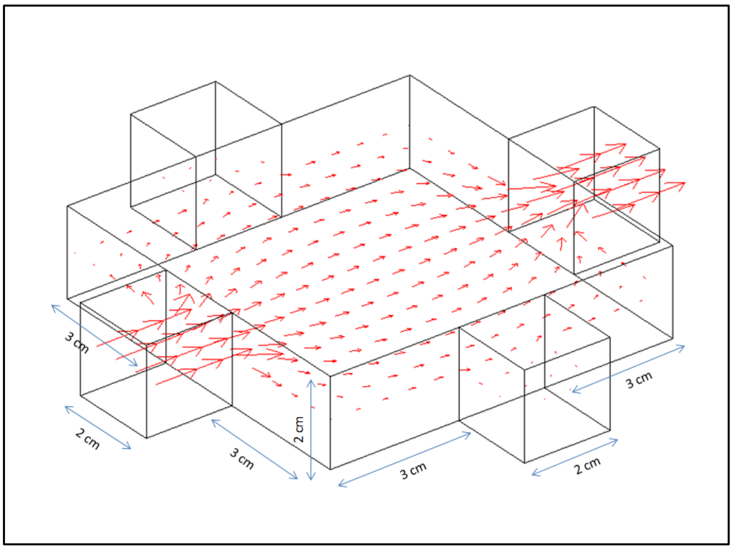

Figure 3.7. The technical drawing with current simulation of the first phantom

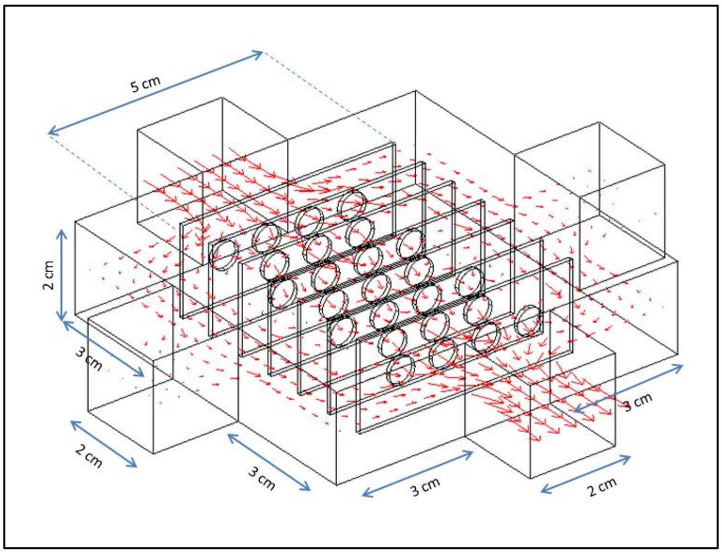

Figure 3.8. The technical drawing with current simulation of the second phantom

The front view and oblique view photographs of the manufactured phantom structure are shown in Figure 3.9 and Figure **3.10**, respectively.

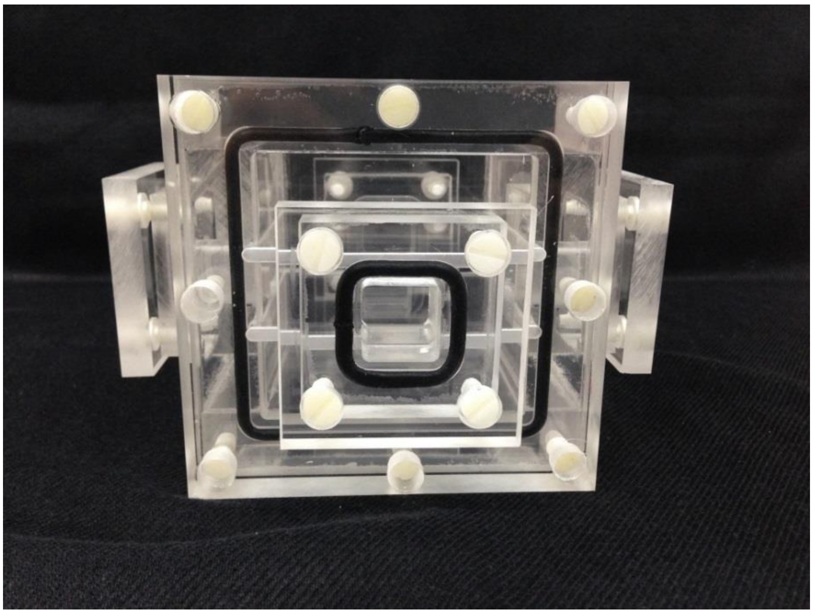

Figure 3.9. The front view photograph of the manufactured phantom structure [70]

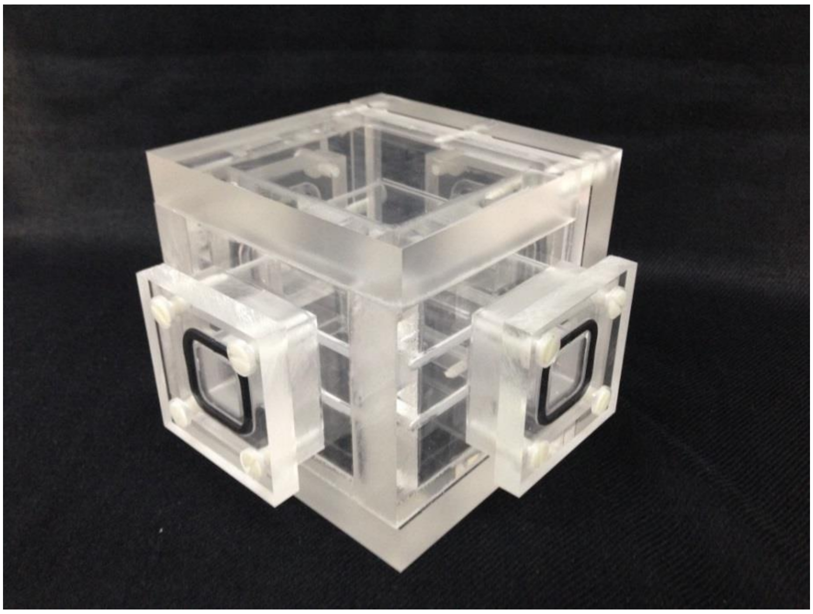

Figure 3.10. The oblique view photograph of the manufactured phantom structure [70]

The experimental data obtained from the first phantom is used for reconstructing 2D current density distribution in transverse plane. This data is also used for comparing the total injected current with total integrated current from the reconstructed current density image. As shown in Figure 3.7, the current density in z direction is kept as zero by placing two insulating layers horizontally with a distance which is equal to the width of the electrodes.

The experimental data obtained from the second phantom is used for visual observation of changes in direction of the current density vectors due to the insulating layers with circular holes. The insulating layers have different number of circular holes as shown in Figure 3.8. By the arrangement of the insulating layers, the variation of the direction of the current density vectors is achieved. Both of the phantoms are filled with the subdomain solution of 0.1gr $CuSO_4$ and 0.145gr NaCl dissolved in 100ml pure water to obtain conductivity of 0.2 S/m which is approximately equal to the conductivity of blood [71].

CHAPTER 4

RESULTS AND DISCUSSION

4.1 Introduction

In this chapter, accuracy of the developed programmable current source is investigated, and reconstructed magnetic flux density and current density images of MRCDI experiments, which are explained in Chapter 3, are presented. First, the performance of current source under different load conditions is given. Then, the images of uniform phantom experiment are given and discussed. Afterwards, the images of with current steering insulator object experiment are presented. Finally, an experiment for determining the minimum measurable current density with UMRAM 3T MRI system is explained and the results of the experiment are discussed.

4.2 Results of the Programmable Current Source

In order to test the performance of the programmable current source, the current source is programmed to inject current in different levels of amplitude and pulse-width. The amplitude measurement experiments are repeated for different resistive loads. The pulse-width measurement experiments are performed for only 1kOhm resistive load. The amplitude values of the measured output currents are tabulated in Table 4.1. In addition, the pulse-width measurements are tabulated in Table 4.2.

Table 4.1. Amplitude of the measured output current values for different load conditions

I / R	***1Ohm***	***10Ohm***	***100Ohm***	***470Ohm***	***1kOhm***	***2kOhm***
1mA	1.00	1.01	1.02	1.04	1.13	1.08
5mA	4.40	4.45	4.44	4.49	4.56	4.57
10mA	9.80	9.64	9.62	9.70	9.79	9.85
20mA	19.20	19.15	19.05	19.17	19.28	19.41
50mA	49.30	49.48	49.13	49.32	49.50	49.70
100mA	98.20	98.92	98.32	98.80	99.06	99.20

Table 4.2. Pulse-width measurements of the output current for 1kOhm resistive load

Input Δt (ms)	***Measured Δt (ms)***	***Error Δt (ms)***	***Error %***
1ms	1.10ms	0.10ms	10%
5ms	4.80ms	0.20ms	4%
10ms	9.45ms	0.55ms	5.5%
20ms	19.10ms	0.90ms	4.5%
50ms	48.80ms	1.20ms	2.4%

Considering measured amplitude values of the output current, which are given in Table 4.1, the maximum error is 1.8mA when the input amplitude is 100mA. The error corresponds to 1.8% of the input amplitude, and the experiment is perfomed when the load resistance is 1Ohm. Also, even for the input amplitude is as low as 1mA, the amplitude error is less than 0.13mA, which corresponds to 13% of the input amplitude.

The output voltage of the 3.3V regulator, which is used in DC regulator, is 3.37V. Also, the current sensing resistor of the V-I converter, is 15Ohm. Therefore, the maximum output current capability of the the current source is 3.37V/15Ohm = 224.7mA. This maximum current can be injected to any load as long as necessary physical conditions are satisfied. The designed step-up DC-DC convertor is capable of producing output voltages as high as 250V. Therefore, considering the voltage drop in relays and MOSFET in the V-I converter, 224.7mA DC can be injected to 1kOhm resistive load at maximum. In order to evaluate the consistency of the measured output current values, the amplitude resolution of the current source must be determined. As the DAC is 8-bit, the amplitude resolution of the current source is 224.7mA/256 =878uA. When considering the amplitude resolution, the measured amplitude values given in Table 4.1 are consistent.

The temporal accuracy of the current source is evaluated by measuring the Δt_2 values of the output current for different user-defined inputs. The maximum temporal error is 1.2ms, when Δt_2 = 50ms is selected, which corresponds to 2.4% temporal error. Also, even when Δt_2 = 1ms is selected, the temporal error is less than 10%. The error values are presumed to be due to the experimental errors and SSR latency.

Also, one of the features of the programmable current source is the possibility of changing the frequency of the output current. The designed and implemented programmable current source is capable of generating the current waveform in 0-300Hz frequency range without any distortion. The oscillogram of 50mA-DC and

50mA-50Hz output current when Δt_2 = 100ms, and Δt_4 = 50ms are given in Figure 4.1 and Figure 4.2, respectively. The measurements are performed when the load resistance is 1kOhm. The rise time and fall and the fall time of the current pulse is are measured as 120us and 3us, respectively.

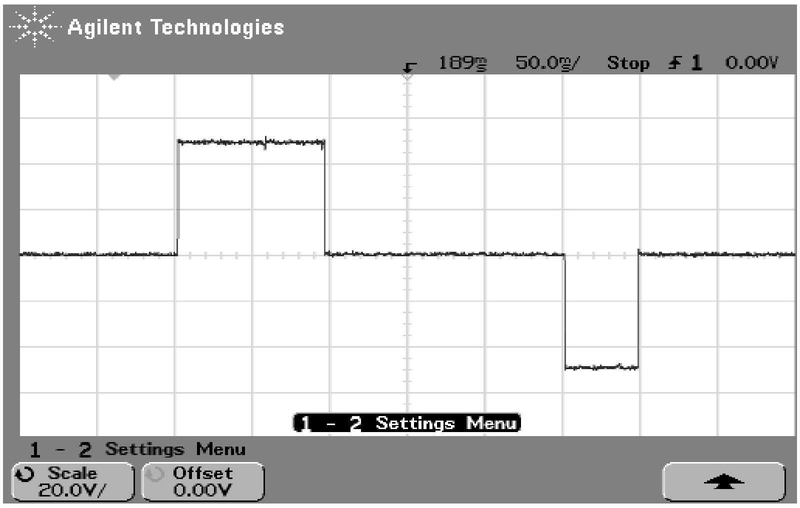

Figure 4.1. The oscillogram of 50mA-DC output current with 100ms and 50ms forward and inverse pulse-width, injected to 1kOhm resistive load

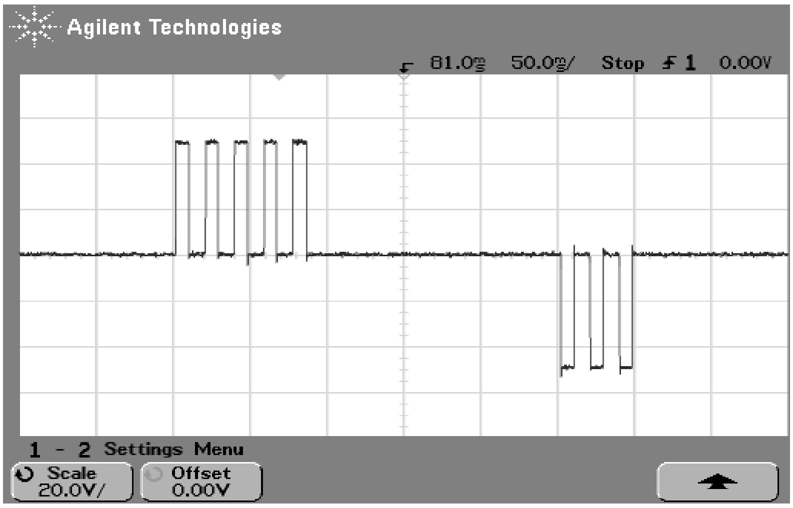

Figure 4.2. The oscillogram of 50mA-50Hz output current with 100ms and 50ms forward and inverse pulse-width, injected to 1kOhm resistive load

4.3 Experiment with the Uniform Phantom

In Chapter 3, the uniform phantom is explained in detail. In this section, magnetic flux density and current density images for 20mA-DC, and $\Delta t_2 = \Delta t_4 = 20$ms current injection, which is in +x direction, are given. FOV is 128mmx128mm. Slice thickness is 5mm. Base resolution is 64. The number of averaging is 32. TR=250ms, and TE=60ms. The simulation and the experimental results of the z-component of the magnetic flux density measurement, $B_z(x, y)$ are shown in Figure 4.3. The simulation and experimental results of the x-component of the magnetic flux density measurement, $B_x^+(x, y)$ for z = 7.5mm, and $B_x^-(x, y)$ for z = -7.5mm are shown in Figure 4.4. The simulation and experimental results of the y-component of the magnetic flux density measurement, $B_y^+(x, y)$ for z = 7.5mm, and $B_y^-(x, y)$ for z = -7.5mm are shown in Figure 4.5. From these magnetic flux density measurements, the current density distribution is reconstructed. The x-component of the current density distribution, and the y-component of the current density distribution are shown in Figure 4.6. The arrow plot is shown in Figure 4.7. Also the streamline plot is shown in Figure 4.8.

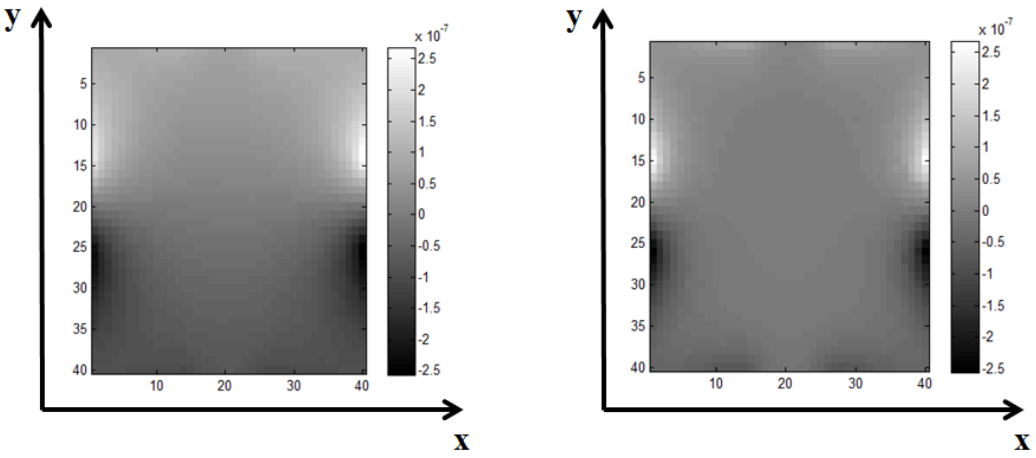

(a) **(b)**

Figure 4.3. The z-component of the magnetic flux density measurement, $\boldsymbol{B_z(x, y)}$: (a) The experimental result, (b) The simulation result

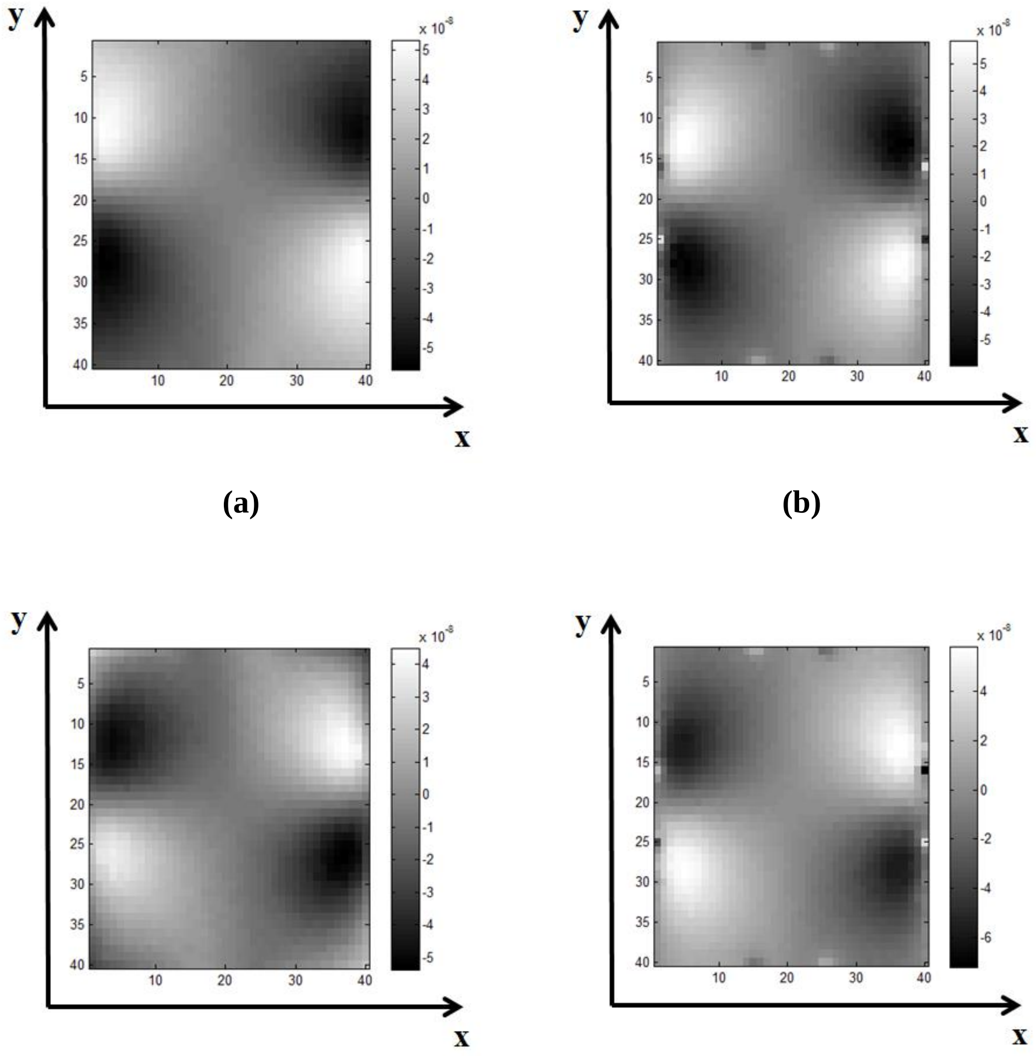

(a) (b)

(c) (d)

Figure 4.4. The x-component of the magnetic flux density measurement : (a) The experimental result for z = 7.5mm, $\boldsymbol{B}_x^+(\boldsymbol{x},\boldsymbol{y})$, (b) The simulation result for z = 7.5mm, $\boldsymbol{B}_x^+(\boldsymbol{x},\boldsymbol{y})$**,** (c) The experimental result for z = -7.5mm, $\boldsymbol{B}_x^-(\boldsymbol{x},\boldsymbol{y})$**,** (d) The simulation result for z = -7.5mm, $\boldsymbol{B}_x^-(\boldsymbol{x},\boldsymbol{y})$

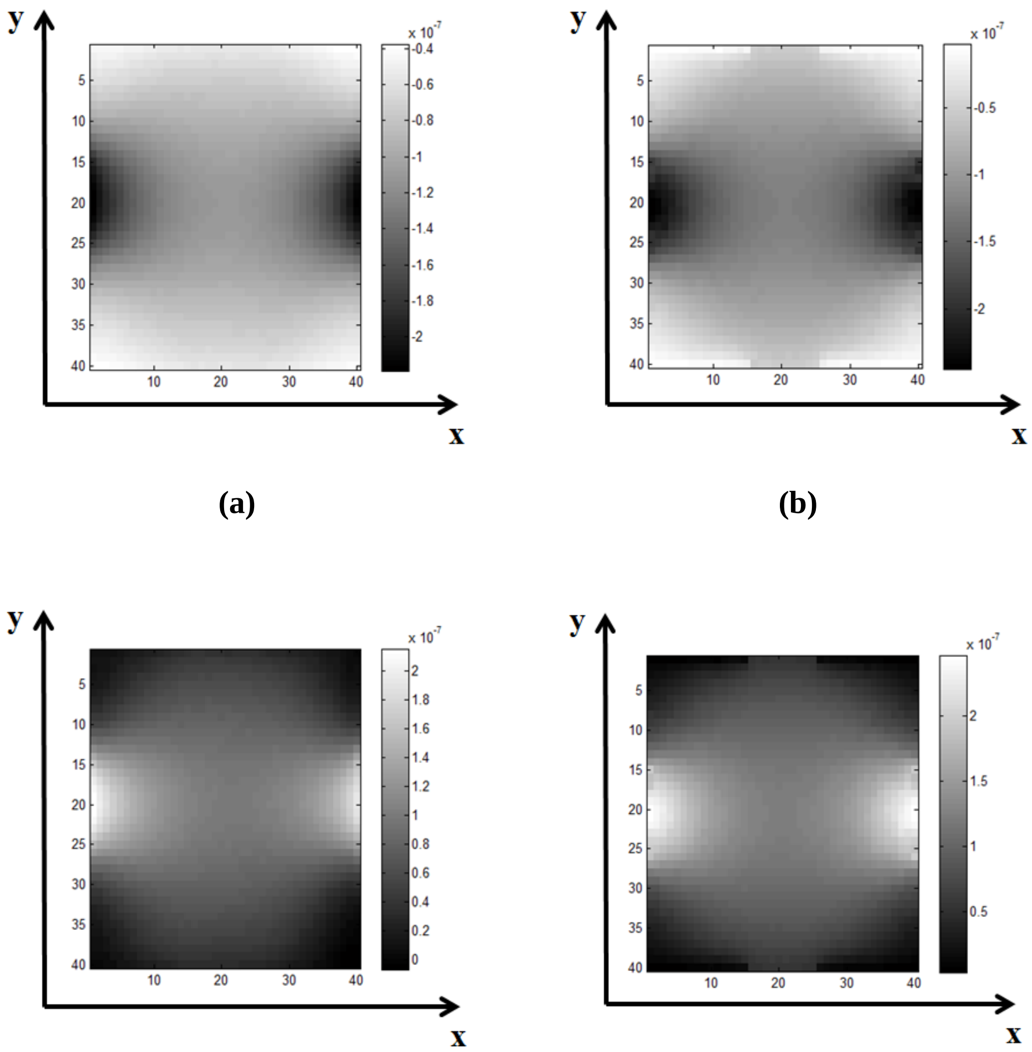

(a) **(b)**

(c) **(d)**

Figure 4.5. The y-component of the magnetic flux density measurement : (a) The experimental result for z = 7.5mm, $\boldsymbol{B_y^+(x,y)}$, (b) The simulation result for z = 7.5mm, $\boldsymbol{B_y^+(x,y)}$**,** (c) The experimental result for z = -7.5mm, $\boldsymbol{B_y^-(x,y)}$**,** (d) The simulation result for z = -7.5mm, $\boldsymbol{B_y^-(x,y)}$

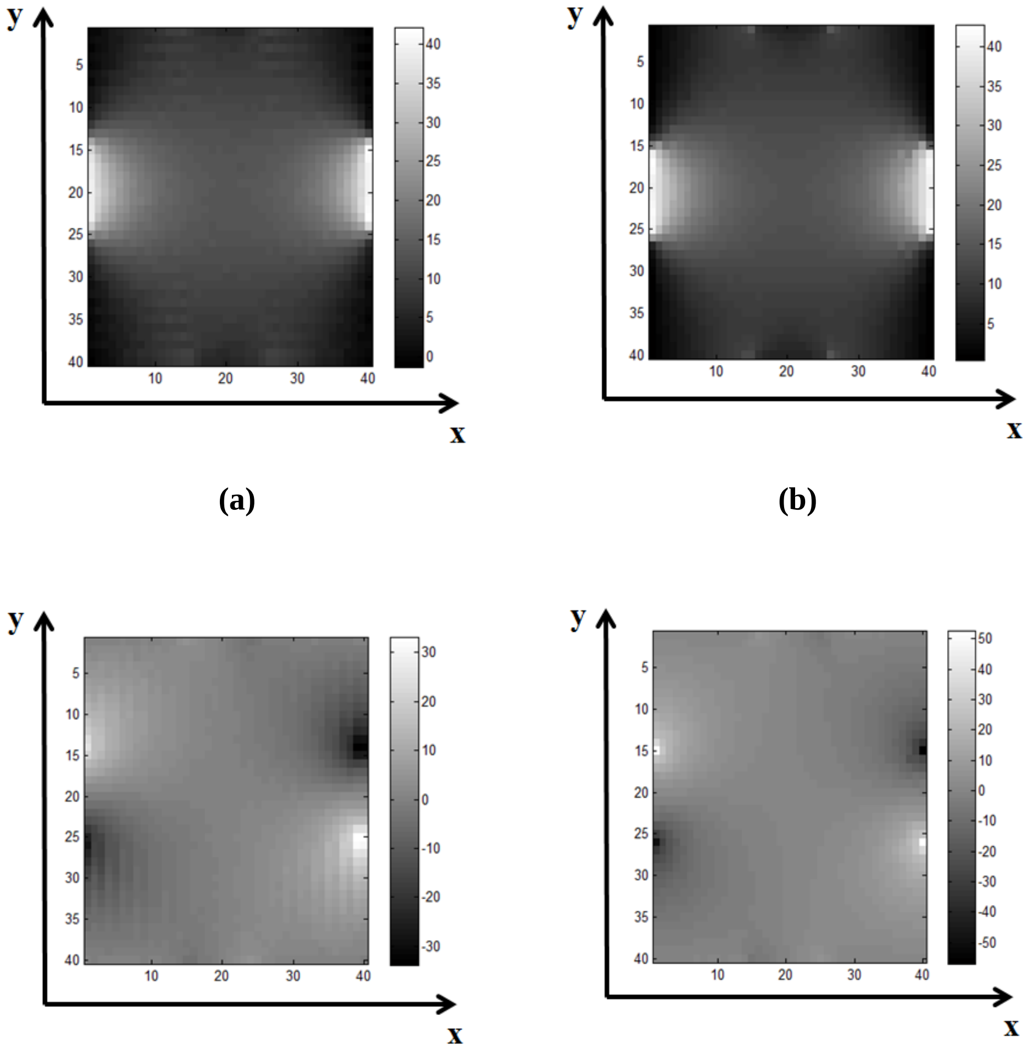

(a) (b)

(c) (d)

Figure 4.6. The reconstructed current density measurement : (a) The experimental result of the x-component of the current density distribution, $\boldsymbol{J_x(x,y)}$, (b) The simulation result of the x-component of the current density distribution, $\boldsymbol{J_x(x,y)}$, (c) The experimental result of the y-component of the current density distribution, $\boldsymbol{J_y(x,y)}$, (d) The simulation result of the y-component of the current density distribution, $\boldsymbol{J_y(x,y)}$

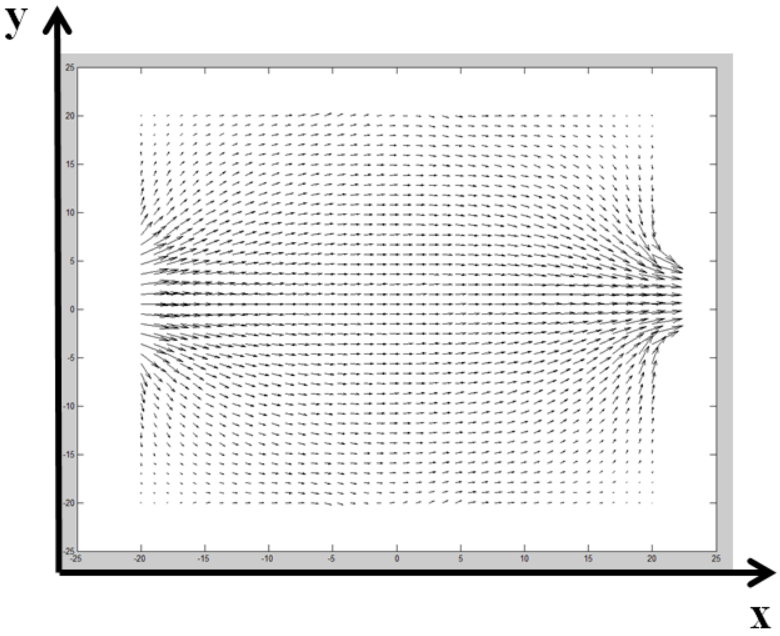

Figure 4.7. The arrow plot of the current density distribution

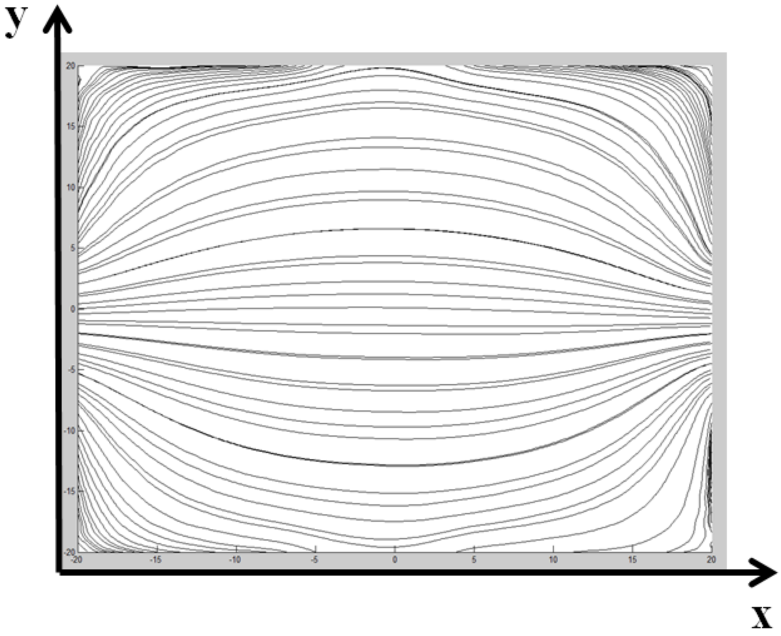

Figure 4.8. The streamline plot of the current density distribution

As shown in Figure 4.3, the z-component of the magnetic flux density distribution is maximum near the electrodes, because higher current density values exist near the electrodes. Upper part of the magnetic flux density image is brighter, whereas lower part of the magnetic flux density image is darker. The brighter regions correspond to the magnetic flux in +z direction and the darker regions correspond to the magnetic flux in –z direction.

As shown in Figure 4.4, magnitude of the x-component of the magnetic flux density distribution gets the highest value when magnitude of the y-component of the current density is maximum which corresponds to the regions near the electrodes. In a similar manner, as shown in Figure 4.5, magnitude of the y-component of the magnetic flux density distribution gets its highest value when magnitude of the x-component of the current density is maximum which corresponds to the regions near the electrodes and midline of the image.

As shown in Figure 4.6, the x-component of the current density is highest near the electrodes, and becomes uniform for farther regions. In the regions near the source electrode, the y-component of the current density has positive values for upper side of the image and has negative values for lower side of the image. Similarly, in the regions near the sink electrode, the y-component of the current density has negative values for upper side of the image and has positive values for lower side of the image. This is expected, as the current flows out from the source electrode, flows into the sink electrode. The arrow plot and the streamline plot of the current density is also shown in Figure 4.7 and Figure 4.8. In Figure 4.7, the length of arrows is correlated with the magnitude of the current density. As shown in Figure 4.7, higher current density exists near the electrodes.

All of the experimental results are compared with the simulation results. The consistency in the results demonstrates the accuracy of the MRCDI experiment.

4.4 Error Analysis of the Uniform Phantom Experiment

In literature, the accuracy of the current density measurement in a uniform phantom is checked by two methods. In the first method, the current density is reconstructed in a cross-sectional area then the surface integral of the current is calculated and compared with the total injected current. In the second method, the magnetic flux density components of cross-sectional area are measured , then the line integral of a closed loop enclosing the cross-sectional area is calculated and compared with the total injecting current [16], [48]. In this study, the first method is used. The cross-sectional area, in which the current density is integrated, is shown in Figure 4.9, as shaded area. The cross-sectional area is an arbitrary one, because the surface integral of the current density in any cross-sectional area should be equal to the total injected current.

To perform the surface integral, an arbitrary column vector of the x-component of the current density is chosen, due to that the x-component of the current density is the orthogonal component to the selected cross-sectional area. As the current is constrained between two insulating layer with a distance equal to the width of the electrode, the selected column vectors are uniform in z-direction. The voxel size is 2mmx2mmx5mm and the width of the phantom is 8cm. Therefore, the column vector is consisted of 40 current density values. The matrix representation of the selected cross-sectional area is shown in Figure 4.10. Therefore, the total current passes through the cross-sectional area is expressed as given in (4.1).

$$I_{total} = \int_S J(y) \cdot dydz = \int_0^{2cm} \left(\sum_{i=1}^{40} J_i \cdot \Delta y \right) dz \tag{4.1}$$

As given in (4.1), the total current passing through the selected cross-sectional area is calculated by summing all values in the selected arbitrary column vector, which are multiplied with the pixel width, and multiplying it with the height of the phantom. The calculated current must be equal to the total injected current.

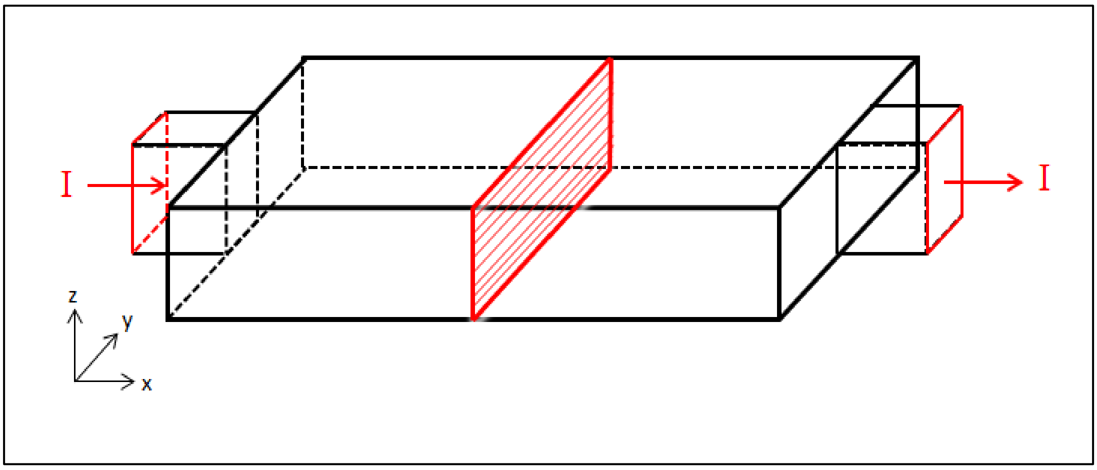

Figure 4.9. The drawing of the designed phantom and the cross-sectional area in which the current density is integrated

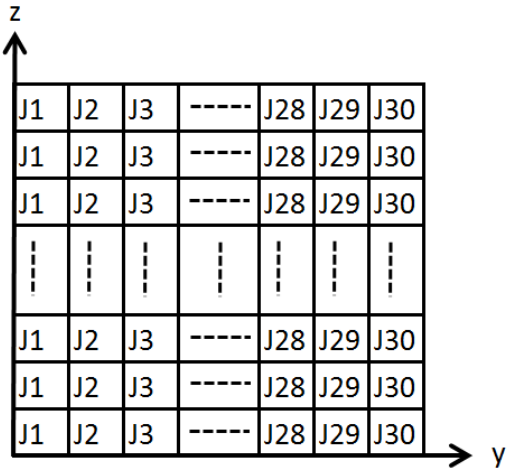

J1	J2	J3	-----	J28	J29	J30
J1	J2	J3	-----	J28	J29	J30
J1	J2	J3	-----	J28	J29	J30
¦	¦	¦	¦	¦	¦	¦
J1	J2	J3	-----	J28	J29	J30
J1	J2	J3	-----	J28	J29	J30
J1	J2	J3	-----	J28	J29	J30

Figure 4.10. Matrix representation of the selected cross-sectional area

For checking the accuracy of the measurement, 12th column vector of the x-component of the current density image is selected. Corresponding calculated total current is expressed as given in (4.2).

$$I_{total} = \int_0^{2cm} \left(\sum_{i=1}^{40} J_i \cdot \Delta y \right) dz = \int_0^{2cm} 463.23uA/mm^2 \cdot 2mm \; dz = 18.52\text{mA} \quad (4.2)$$

The total injected current is 20mA. The calculated current from the reconstructed current density image is 18.52mA, which is approxiamately equal to the total injected current. The total experimental error is 7.4%. The total error is also calculated for different number of averaging. The results are given in Table 4.3.

Table 4.3. The calculated error results for different number of averaging

N_{avg}	I_{total} *(mA)*	$I_{calculated}$ *(mA)*	I_{error} *(mA)*	*Error %*
8	20mA	18.42mA	1.58mA	7.9%
16	20mA	18.48mA	1.52mA	7.6%
32	20mA	18.52mA	1.48mA	7.4%

As given in Table 4.3, increasing the number of averages decreases the random noise of the system [16].

4.5 Experiment with the Uniform Phantom with Current Steering Object

In this experiment, the observation of change in current flow is aimed. For this purpose, the uniform phantom with a current steering insulator object is used. The MRCDI output images for 20mA-DC, and $\Delta t_2 = \Delta t_4 =$20ms current injection, which is in -y direction, are given. FOV is 128mmx128mm. Slice thickness is 5mm. Base resolution is 64. Number of averaging is 16. TR=250ms, and TE=60ms. The simulation and the experimental results of the z-component of the magnetic flux density measurement, $B_z(x,y)$ are shown in Figure 4.11. The simulation and experimental results of the x-component of the magnetic flux density measurement, $B_x^+(x,y)$ for z = 7.5mm, and $B_x^-(x,y)$ for z = -7.5mm are shown in Figure 4.12. The simulation and experimental results of the y-component of the magnetic flux density measurement, $B_y^+(x,y)$ for z = 7.5mm, and $B_y^-(x,y)$ for z = -7.5mm are shown in

Figure 4.13. From these magnetic flux density measurements, the current density distribution is reconstructed. The x-component of the current density distribution, and the y-component of the current density distribution are shown in Figure 4.14. The arrow plot is shown in Figure 4.15.

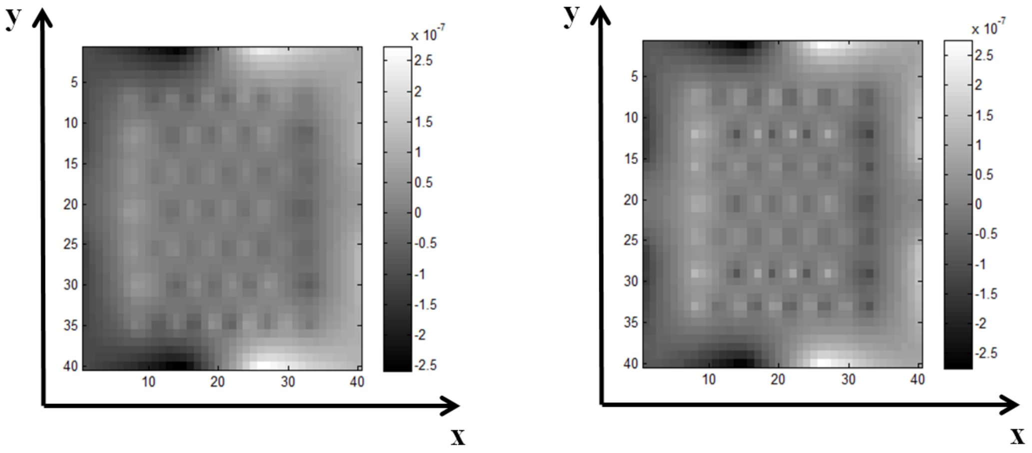

(a) **(b)**

Figure 4.11. The z-component of the magnetic flux density measurement : (a) The experimental result, $\boldsymbol{B_z(x,y)}$, (b) The simulation result, $\boldsymbol{B_z(x,y)}$

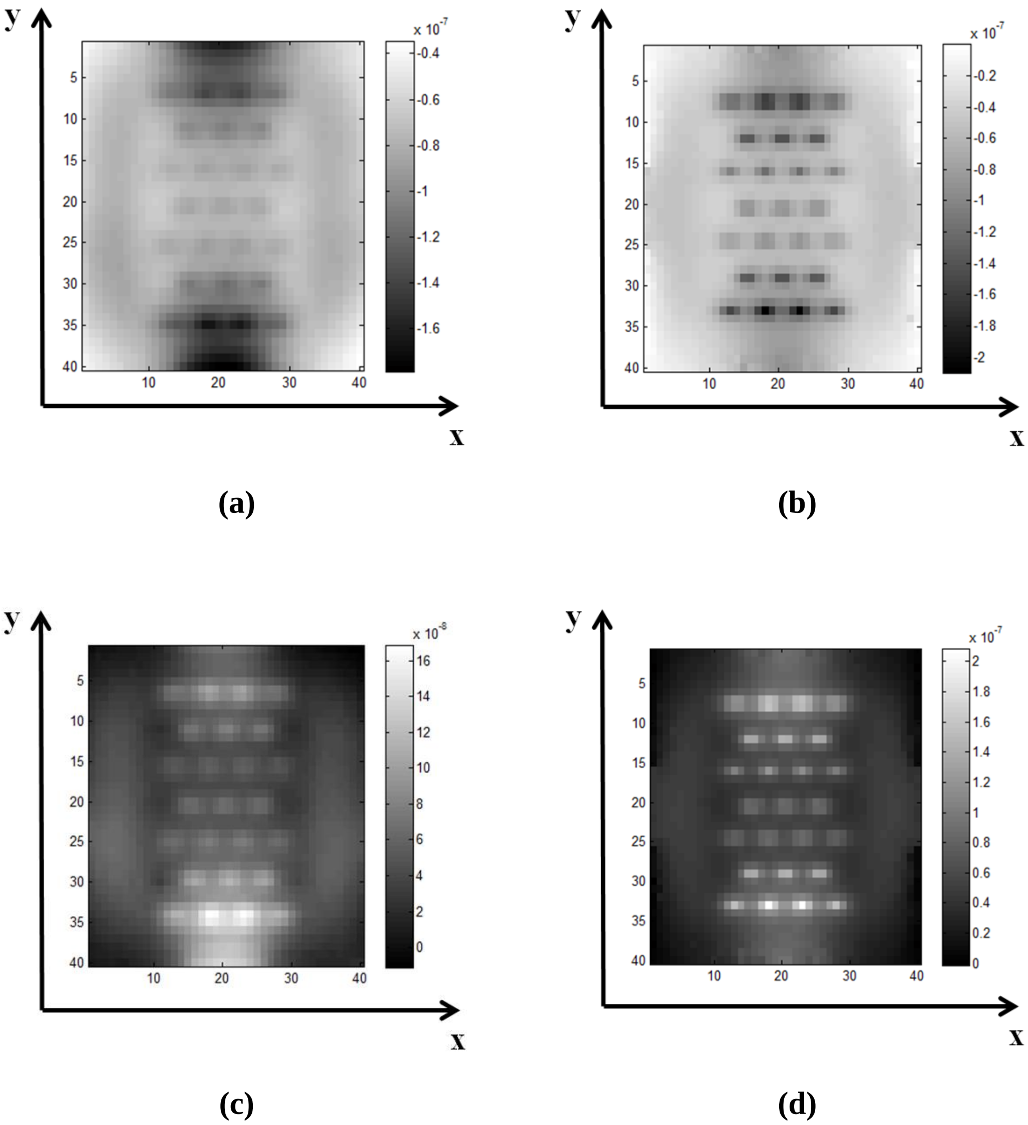

(a) (b)

(c) (d)

Figure 4.12. The x-component of the magnetic flux density measurement : (a) The experimental result for z = 3mm, $\boldsymbol{B_x^+(x,y)}$, (b) The simulation result for z = 3mm, $\boldsymbol{B_x^+(x,y)}$, (c) The experimental result for z = -3mm, $\boldsymbol{B_x^-(x,y)}$, (d) The simulation result for z = -3mm, $\boldsymbol{B_x^-(x,y)}$

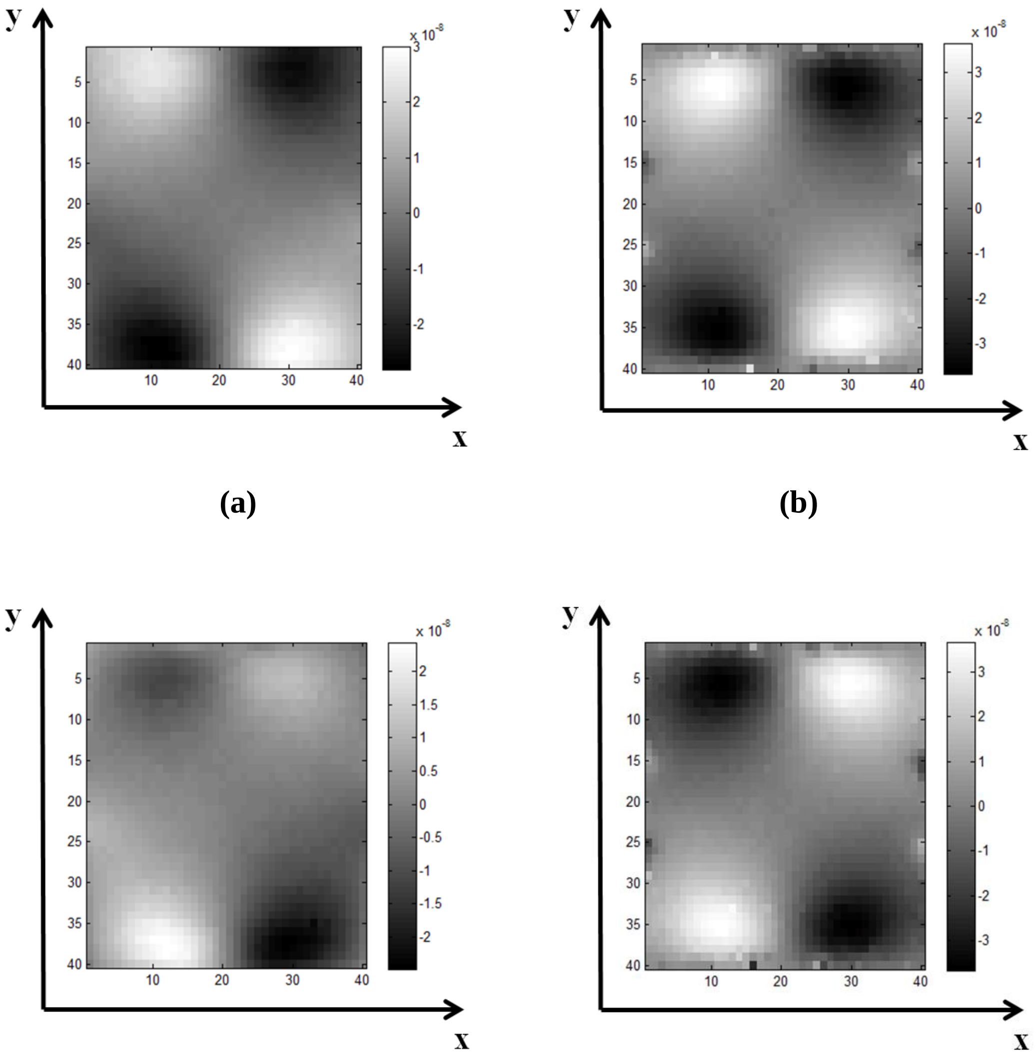

(a)

(b)

(c)

(d)

Figure 4.13. The y-component of the magnetic flux density measurement : (a) The experimental result for z = 3mm, $\boldsymbol{B}_y^{+}(\boldsymbol{x},\boldsymbol{y})$, (b) The simulation result for z = 3mm, $\boldsymbol{B}_y^{+}(\boldsymbol{x},\boldsymbol{y})$**,** (c) The experimental result for z = -3mm, $\boldsymbol{B}_y^{-}(\boldsymbol{x},\boldsymbol{y})$**,** (d) The simulation result for z = -3mm, $\boldsymbol{B}_y^{-}(\boldsymbol{x},\boldsymbol{y})$

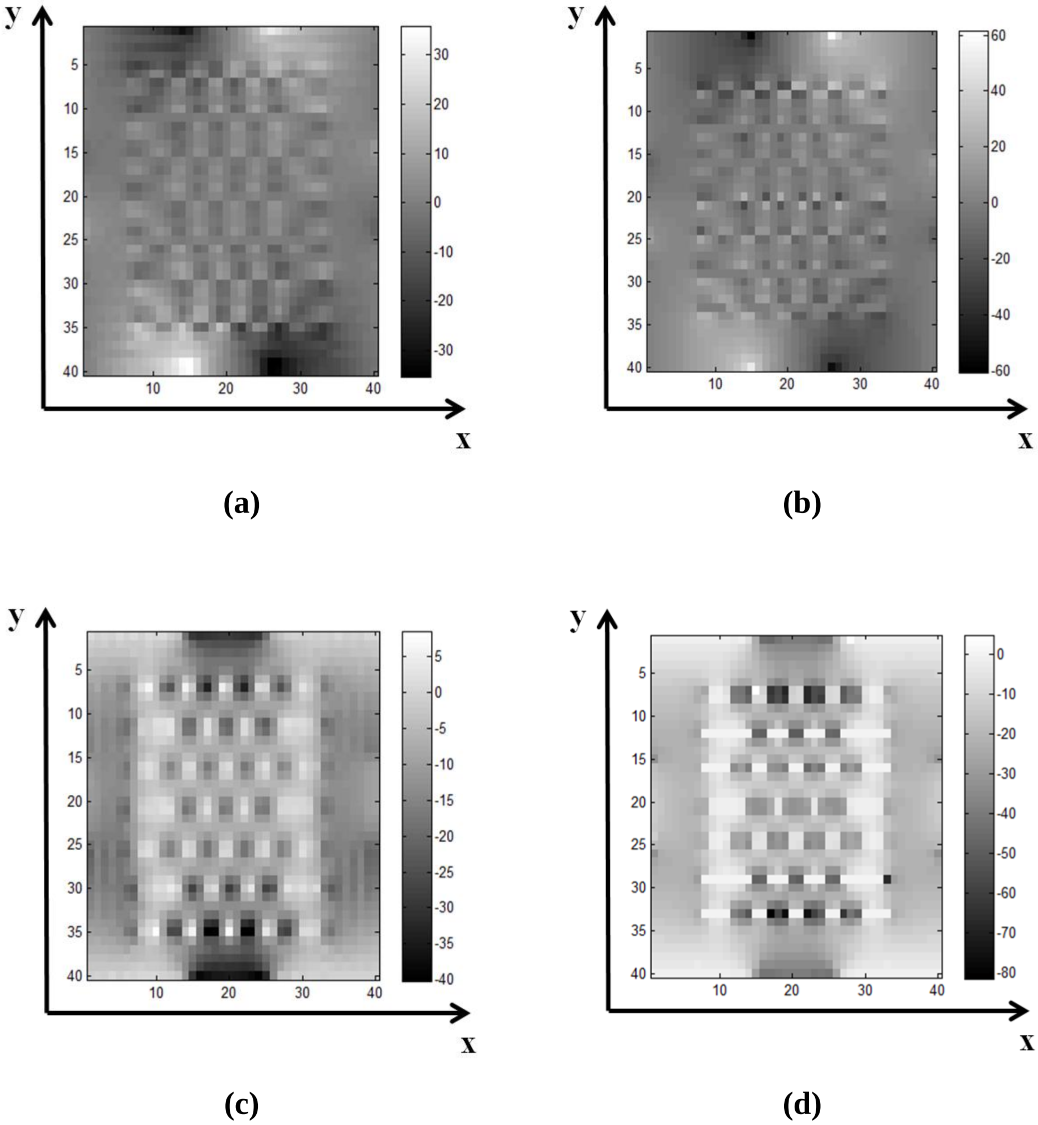

(a) (b) (c) (d)

Figure 4.14. The reconstructed current density measurement : (a) The experimental result of the x-component of the current density distribution, $\boldsymbol{J_x(x,y)}$, (b) The simulation result of the x-component of the current density distribution, $\boldsymbol{J_x(x,y)}$, (c) The experimental result of the y-component of the current density distribution, $\boldsymbol{J_y(x,y)}$, (d) The simulation result of the y-component of the current density distribution, $\boldsymbol{J_y(x,y)}$

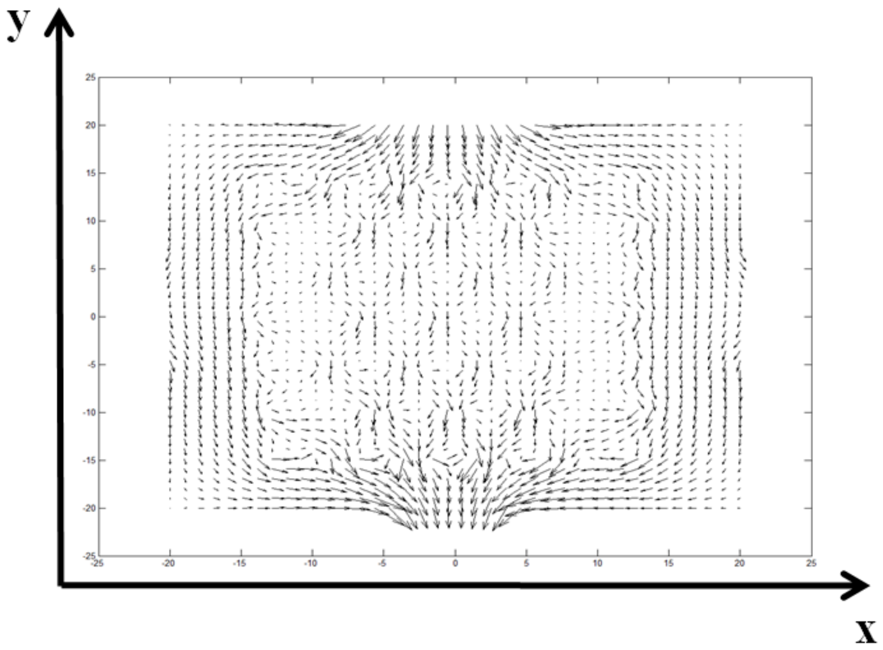

Figure 4.15. The arrow plot of the current density distribution

As shown in Figure 4.11, the z-component of the magnetic flux density distribution is maximum near the electrodes. This is expected, as the highest current density values exist near the electrodes. Also the z-component of magnetic flux density values are higher near the circular holes. This is also expected, as the current is forced to flow into the circular holes. Therefore, higher current density distribution causes the higher magnetic flux density values. In addition, right side of the magnetic flux density image is brighter, whereas left side of the magnetic flux density image is darker. The brighter regions correspond to the magnetic flux in +z direction and the darker regions correspond to the magnetic flux in –z direction. These results verify the current flow in –y direction.

As shown in Figure 4.12, the magnitude of the x-component of the magnetic flux density distribution gets the highest value when magnitude of the y-component and z-component of the current density is the maximum which corresponds to the regions near the electrodes and circular holes. In a similar manner, as shown in

Figure 4.13, magnitude of the y-component of the magnetic flux density distribution gets the highest value when magnitude of the x-component and the z-component of the current density is maximum. However, the magnitude of the x-component of the current density is significantly higher near to electrodes than farther regions. Therefore, the circular holes could not be observed.

As shown in Figure 4.14, the x-component of the current density has the highest values near the electrodes, and near the edges of the circular holes. In the regions near the source electrode, the x-component of the current density has positive values for right side of the image and has negative values for left side of the image. Similarly, in the regions near the sink electrode the x-component of the current density has negative values for right side of the image and has negative values for left side of the image. This is expected, as the current flows out from the source electrode, spreads out, leaks into the circular holes, and then flows into the sink electrode. As shown in Figure 4.14, the y-component of the current density is almost zero between the insulating layers, and is high near the circular holes. The current flow is also shown in Figure 4.15. Length of the arrows is correlated with the magnitude of the current density. The change in the current flow in the territory of the circular holes is visible.

4.6 Experiment for Measuring the Minimum Measurable Current Density with UMRAM 3T MRI System

In this experiment, the minimum measurable current density with UMRAM 3T MRI system is investigated. For this purpose, the inherited noise of the system must be known. One way of determining this, is calculating the standard deviation of the magnetic flux density images. In order to image the current density distribution with MRCDI, the injected current must accumulate additional magnetic flux density which is greater than the calculated standard deviation of the magnetic flux densities.

To achieve the minimum measurable current density value, 32 phase images are acquired for each orientation, when the slice thickness is 5mm. As the inherited noise of the system is investigated, the experiments are performed without currrent injection. All magnetic flux density images are calculated for $\Delta t_2 = \Delta t_4$ = 20ms. The standard deviation of each pixel in 32 different $B_z(x,y)$, $B_x^+(x,y)$, $B_x^-(x,y)$, $B_y^+(x,y)$, and $B_y^-(x,y)$ images are calculated, and $\Delta B_z(x,y)$, $\Delta B_x^+(x,y)$, $\Delta B_x^-(x,y)$, $\Delta B_y^+(x,y)$, and $\Delta B_y^-(x,y)$ images are formed. Using the formed magnetic flux density images, $\Delta J_x(x,y)$ and $\Delta J_y(x,y)$ images are reconstructed. The total current image is calculated, and the minimum measurable current density value is presumed as the root mean square value of the total current image. The same algorithm is repeated for different number of image sets, which corresponds to the number of averaging of the MRCDI experiment. The calculated results are tabulated in Table 4.4.

Table 4.4. Calculated minimum measurable current density values

# of Avg.	$\boldsymbol{\Delta B_z(x,y)}$ **(nT)**	$\boldsymbol{\Delta B_x^+(x,y)}$ **(nT)**	$\boldsymbol{\Delta B_x^-(x,y)}$ **(nT)**	$\boldsymbol{\Delta B_y^+(x,y)}$ **(nT)**	$\boldsymbol{\Delta B_y^-(x,y)}$ **(nT)**	$\boldsymbol{J_{min}}$ **(uA/mm^2)**
32	3.3457	3.2404	2.4596	2.2165	2.2926	0.2601
16	3.3309	2.9984	2.7403	2.2342	2.1544	0.3520
8	3.3517	2.8956	2.9044	2.2253	2.0938	0.5089
4	3.5536	2.8803	3.2004	2.2532	2.0999	0.8005
2	3.5733	2.7792	3.4471	2.2444	2.1750	1.2252

As given in Table 4.4, the calculated minimum measurable current density value decreases significantly, when increasing the number of averaging. The experimental results indicate that for 32 number of averaging current density values greater than 0.2601uA/mm^2 could be measured with the UMRAM 3T MRI System. By integrating the minimum measurable current density value over the cross-sectional area, the minimum required current injection could be calculated for the designed phantom. The minimum measurable current, which must be injected to the electrode, is expressed as given in (4.3).

$$I_{min} = \iint_S J \cdot dS = 0.2601\text{uA/mm}^2 \cdot 16\text{cm}^2 = 416.16\text{uA} \tag{4.3}$$

CHAPTER 5

CONCLUSION

In this chapter, the work done in this thesis study is summarized. The topology of the designed and implemented current source and the MRCDI experiments are briefly described. The results of the current source is given and discussed. The results of MRCDI experiments are given and discussed.

5.1 Summary of the Thesis Study

In this thesis study, the design and implementation of a constant current source to be used in MRCDI and MREIT applications, and imaging the current density distribution by using 3T MR tomography are aimed. For this purpose, a programmable current source which operated in synchrony with the MRI sequence is designed and implemented. The current source is controlled by an MCU, and output current parameters of the current source which are amplitude, pulse-widths after 90° and 180° RF pulses, delay durations after 90° and 180° RF pulses, and frequency could be determined by user. The connection between the user and the current source is satisfied by an easy-to-use GUI. Also, the current source has four channels. Selection of source and sink channels is possible.

The current source topology can be explained as following. First, the MCU stores the desired output current parameters. When the trigger signal is detected, the MCU generates a control signal according to the stored parameters. The control signal gives the amplitude information of the output current to DAC. The DAC converts this signal to analog, and then sends the analog signal to V-I converter. The analog signal determines the amplitude of the output current. The V-I converter is a simple circuitry consisted of a high voltage OP-AMP and a MOSFET. The interleaved current pulse is generated by a current steering topology. The control signal generated by the MCU, activates and deactivates SSR’s according to the timing parameters. Therefore, the interleaved current waveform is applied to load in synchrony with the MRI sequence. In order to generate higher amplitude output current, the supply voltage of the system is amplified by a step-up DC-DC converter. Also, the protection of the designed circuitries and the MCU is provided by step-up DC-DC converter controller mechanism. This mechanism not only protects the circuitries, but also decreases the power consumption of the overall system.

The designed current source is implemented to be used in MRCDI and MREIT applications. Therefore, the use of the current source is demonstrated by two different MRCDI experiments. The MRCDI algorithm is based on the detection of the phase accumulation due to the externally applied current. The phase image is unwrapped and scaled, so that the magnetic flux density components are acquired. From the acquired magnetic flux density components, the current density distributions are reconstructed by using Ampere’s Law.

In the first experiment, the current density distribution inside a uniform phantom is reconstructed, and the total current is calculated. The calculated total current and the injected total current are compared, so that the accuracy of the MRCDI experiment is demonstrated. In the second experiment, a current steering insulator object is inserted inside the uniform phantom and the current density distribution is reconstructed. The change in current flow is visually observed. All reconstructed current density distributions are compared with the simulation results. Obtained experimental results and the simulation results are consistent.

5.2 Discussions and Conclusions

In the study, the supply voltage of the designed and implemented programmable current source can be increased up to 250V. The maximum current injection of the current source is 224.7mA, when the load resistance is 1kOhm. The amplitude resolution of the current source is 878uA. The current source is experimented with different loads for different input parameters. The output current is measured when the input amplitudes are 1mA, 5mA, 10mA, 20mA, 50mA, and 100mA. The measurements are performed for 1Ohm, 10Ohm, 100Ohm, 470Ohm, 1kOhm, and 2kOhm resistive loads. The maximum amplitude error is calculated as 1,8mA for 100mA current injection, when the load resistance is 1Ohm. Also, even in the current injection as low as 1mA the amplitude error is less than 13%. The temporal accuracy of the current source is evaluated by measuring the pulse-width values after 90° RF pulse. Measurements are performed for different pulse-width inputs, which are 1ms, 5ms, 10ms, 20ms, and 50ms. The maximum temporal error is 1.2ms, when the input pulse-width is 50ms, which corresponds to 2.4%. Also, even when the input pulse-width is 1ms, the temporal error is less than 10%. The error values are presumed to be due to the experimental errors and SSR latency. In the current source, the frequency of the output current can also be determined. The current source is capable of injecting output current in 0-300Hz frequency range without any distortion.

The MRCDI experiments are performed for 20mA-DC, and $\Delta t_1 = \Delta t_2 = 20$ms current injection to uniform phantom and to uniform phantom with current steering insulator object. The experiment with the uniform phantom is performed for FOV is 128mmx128mm, the slice thickness is 5mm, number of averaging is 32, and the voxel size is 2mmx2mmx5mm. From the reconstructed current density distribution of the uniform phantom, the total current is calculated as 18.52mA. The calculated error is 7.4%. In the experiment with the current insulator object, the reconstructed current density images, and current density vectors clearly indicate the change in the current flow near circular holes. Also, an experiment for the detection of the minimum measurable current with UMRAM 3T MRI system is performed. The minimum measurable current density is calculated as 0.2601uA/mm^2 for $\Delta t_1 = \Delta t_2 =$ 20ms.

5.3 Publications during MSc. Study

1-) **C. Göksu**, B. M. Eyüboğlu, and H. H. Eroğlu, “A Programmable Current Source for MRCDI & MREIT Applications,” in XIII Mediterranean Conference on Medical and Biological Engineering and Computing 2013 IFMBE Proceedings, 2014, pp. 198–201.

2-) H. H. Eroğlu, B. M. Eyüboğlu, and **C. Göksu**, “Design and implementation of a bipolar current source for MREIT applications,” in XIII Mediterranean Conference on Medical and Biological Engineering and Computing 2013 IFMBE Proceedings, 2014, no. 2, pp. 161–164.

REFERENCES

[1] J. P. Morucci and B. Riguad, “Bioelectrical impedance techniques in medicine part III; Impedance imaging, medical applications,” *Crit. Rev. Biomed. Eng.*, vol. 24, no. 4–6, pp. 655–677, 1996.

[2] C. Göksu, B. M. Eyüboğlu, and H. H. Eroğlu, “A Programmable Current Source for MRCDI & MREIT Applications,” in *XIII Mediterranean Conference on Medical and Biological Engineering and Computing 2013 IFMBE Proceedings*, 2014, pp. 198–201.

[3] E. C. Fear, S. C. Hagness, P. M. Meaney, M. Okoniewski, and M. A. Stuchly, “Enhancing Breast Tumor Detection with Near-Field Imaging,” *IEEE Microw. Mag.*, vol. 3, no. 1, pp. 48–56, 2002.

[4] B. He, *Neural Engineering*. Springer US, 2013.

[5] Y. Kim, J. B. Fahy, and B. J. Tupper, “Optimal electrode designs for electrosurgery, defibrillation, and external cardiac pacing,” *IEEE Trans. Biomed. Eng.*, vol. 33, no. 9, pp. 845–53, 1986.

[6] D. Tapio and A. Hymes, *New frontiers in TENS (transcutaneous electrical nerve stimulation)*. Minnetonka, Minn. : LecTec Corp., 1987.

[7] B. M. Eyüboğlu, “MAGNETIC RESONANCE CURRENT DENSITY IMAGING,” *WILEY-Encyclopedia Biomed. Eng. WILEY-Encyclopedia Biomed. Eng. (Metin Akay, ed.)*, vol. 4, pp. 2147–2153, 2006.

[8] M. L. G. Joy, “MR current density and conductivity imaging: the state of the art.,” in *Conf Proc IEEE Eng Med Biol Soc.*, 2004, vol. 7, pp. 5315–9.

[9] M. Holz and C. Müller, “Direct Measurement of Single lonic Drift Velocities in Electrolyte Solutions. An NMR Method,” *Berichte der Bunsengesellschaft für Phys. Chemie*, vol. 86, no. 2, pp. 141–147, 1982.

[10] M. Holz and C. Müller, “NMR Measurements of Internal Magnetic Field Gradients Caused by the Presence of an Electric Current in an Electrolyte Solution,” *J. Magn. Reson.*, vol. 40, pp. 595–599, 1980.

[11] A. A. Maudsley, H. E. Simon, and S. K. Hilal, “Magnetic field measurement by NMR imaging,” *J. Phys. E.*, vol. 17, no. 3, pp. 216–220, 1984.

[12] B. J. Roth, N. G. Sepulveda, and J. P. Wikswo, “Using a magnetometer to image a two-dimensional current distribution,” *J. Appl. Phys.*, vol. 65, no. 1, pp. 361–372, 1989.

[13] M. Joy, G. Scott, and M. Henkelman, “Invivo Detection of Applied Electric Currents by MRI _ M. Joy, G. Scott and M. Henkelman.pdf,” *Magn. Reson. Imaging*, vol. 7, pp. 89–94, 1989.

[14] P. Pesikan, M. L. G. Joy, G. C. Scott, and R. M. Henkelman, “Two-dimensional current density imaging,” *IEEE Trans. Instrum. Meas.*, vol. 39, no. 6, pp. 1048–1053, 1990.

[15] G. C. Scott and M. L. G. Joy, “Measurement of nonuniform current density by magnetic resonance,” *IEEE Trans. Med. Imaging*, vol. 10, no. 3, pp. 362–374, 1991.

[16] G. C. Scott, M. L. G. Joy, R. L. Armstrong, and R. M. Henkelman, “Sensitivity of magnetic-resonance current-density imaging,” *J. Magn. Reson.*, vol. 97, no. 2, pp. 235–254, 1992.

[17] I. Sersa, K. Beravs, N. J. Dodd, S. Zhao, D. Miklavcic, and F. Demsar, “Electric current density imaging of mice tumors.,” *Magn. Reson. Med.*, vol. 37, no. 3, pp. 404–9, Mar. 1997.

[18] K. Beravs, D. White, I. Sersa, and F. Demsar, “Electric Current Density Imaging of Bone by MRI,” *Magn. Reson. Imaging*, vol. 15, no. 8, pp. 909–915, 1997.

[19] H. R. Gamba and D. T. Delpy, “Artefacts in MR images of electrical current distribution.,” *Phys. Med. Biol.*, vol. 42, no. 12, pp. 2481–91, Dec. 1997.

[20] K. Beravs, A. Demsar, and F. Demsar, “Magnetic Resonance Current Density Imaging of Chemical Processes and Reactions,” *J. Magn. Reson.*, vol. 137, no. 1, pp. 253–257, 1999.

[21] H. R. Gamba and D. T. Delphy, “Measurement Of Electrical Current Density Distribution In A Simple Head Phantom with Magnetic Resonance Imaging,” *Med. Biol. Eng. Comput.*, vol. 36, no. 2, pp. 165–170, 1998.

[22] M. L. Joy, V. P. Lebedev, and J. S. Gati, “Imaging of current density and current pathways in rabbit brain during transcranial electrostimulation,” *IEEE Trans. Biomed. Eng.*, vol. 46, no. 9, pp. 1139–49, Sep. 1999.

[23] O. Özbek, Ö. Birgul, B. M. Eyüboğlu, and Y. Z. Ider, “Imaging Electrical Current Density Using 0.15T Magnetic Resonance Imaging System,” in *Annual International Conference of the IEEE Engineering in Medicine and Biology Society - EMBC*, 2001, no. 5, pp. 2292–2295.

[24] T. P. DeMonte, R. S. Yoon, K. F. Hasanov, D. B. Jorgenson, and M. L. G. Joy, “Image distortion and image mis-registration in low frequency current density imaging,” in *Engineering in Medicine and Biology, 2002. 24th Annual Conference and the Annual Fall Meeting of the Biomedical Engineering Society EMBS/BMES Conference, 2002. Proceedings of the Second Joint*, 2002, vol. 2, no. 1, pp. 933–934.

[25] T. P. Demonte, R. S. Yoon, D. B. Jorgenson, and M. L. G. Joy, “Artifacts Associated with Measuring Cardiac Electrical Currents in a Post-mortem Pig Using Current Density Imaging,” in *Proc. 10th Annu. ISMRM Int. Conf. 2002.*, 2002.

[26] S. Hoon Oh, I. Kon Chun, S. Yeol Lee, M. Hyoung Cho, and C. Woong Mun, “A single current density component imaging by MRCDI without subject rotations,” *Magn. Reson. Imaging*, vol. 21, no. 9, pp. 1023–1028, Nov. 2003.

[27] T. P. Demonte, R. S. Yoon, D. B. Jorgenson, and M. L. Joy, “Effects of Gradient Distortion on Low Frequency Current Density Imaging,” in *ISMRM, XI’th Sci. Meet. and Exh., Toronto, Canada*, 2003, p. 1036.

[28] T. P. Demonte, R. S. Yoon, D. B. Jorgensen, and M. L. G. Joy, “A System for In-vivo Cardiac Defibrillation Current Density Imaging in a Pig,” in *Proceedings of the 25" Annual Intemational Conference of the IEEE EMBS Cancun, Mexico September 17-21,2003*, 2003, pp. 175–178.

[29] R. S. Yoon, T. P. Demonte, L. Organ, and M. L. G. Joy, “Study of Current Density Distribution In a Non-invasive Breast Cancer Detection Device,” in *Proceedings of the 25" Annual Intemational Conference of the IEEE EMBS Cancun, Mexico September 17-21,2003*, 2003, pp. 494–496.

[30] R. S. Yoon, T. P. DeMonte, K. F. Hasanov, D. B. Jorgenson, and M. L. G. Joy, “Measurement of thoracic current flow in pigs for the study of defibrillation and cardioversion,” *IEEE Trans. Biomed. Eng.*, vol. 50, no. 10, pp. 1167–73, Oct. 2003.

[31] R. S. Yoon, T. P. Demonte, K. F. Hasanov, D. Jorgenson, and M. L. G. Joy, “Vector Analysis of Current Pathways in Post-mortem Pig Torso,” in *ISMRM, X’th Sci. Meet. and Exh.*, 2002.

[32] R. S. Yoon, T. P. Demonte, D. Jorgenson, and M. L. G. Joy, “Study of current pathways in porcine heart using current density imaging,” in *international society for magnetic resonance in medicine*, 2001, vol. 89, no. 9, p. 686.

[33] R. S. Yoon, T. P. Demonte, M. L. G. Joy, K. F. Hasanov, and D. Jorgenson, “Direct Measurement of Current Pathways Between Defibrillation Electrodes in a Pig,” in *NASPE*, 2002.

[34] T. P. DeMonte, R. S. Yoon, D. B. Jorgenson, and M. L. G. Joy, “Defibrillation current density imaging: comparison of in-vivo and post-mortem measurements in a pig.,” *Conf. Proc. IEEE Eng. Med. Biol. Soc.*, vol. 6, pp. 3968–70, Jan. 2004.

[35] C. X. B. Yan, T. P. DeMonte, and M. L. G. Joy, “Gradient distortion correction for low frequency current density imaging.,” in *Proceedings of the 28th IEEE EMBS Annual International Conference*, 2006, vol. 1, pp. 260–3.

[36] T. P. Demonte, J.-H. Gao, D. Wang, W. Ma, and M. L. Joy, “Investigation of Relationship between Applied Current Amplitude and Measured Current Density Magnitude in a Live Pig,” in *international society for magnetic resonance in medicine*, 2008, vol. 10, no. 3, p. 3061.

[37] T. P. DeMonte, J.-H. Gao, D. Wang, W. Ma, and M. L. G. Joy, “Measurement of current density vectors in a live pig for the study of human electro-muscular incapacitation devices.,” *Annu. Int. Conf. IEEE Eng. Med. Biol. Soc. - EMBS*, vol. 2008, pp. 5842–5, Jan. 2008.

[38] T. P. Demonte, D. Wang, W. Ma, J.-H. Gao, and M. L. G. Joy, “In-vivo Measurement of Relationship Between Applied Current Amplitude And Current Density Magnitude from 10mA to 110mA,” in *Annual International Conference of the IEEE Engineering in Medicine and Biology Society - EMBS*, 2009, pp. 3177–80.

[39] K. S. Kim, T. I. Oh, S. M. Paek, S. H. Oh, E. J. Woo, S. Y. Lee, and J.-H. Yi, “Design and Performance Analysis of Current Source for 3.0T MREIT System,” *J. Biomed. Eng. Res.*, vol. 25, no. 3, pp. 165–169, 2004.

[40] M. Goharian, K. Chin, and G. R. Moran, “A Novel Microcontroller Current Driver Design for Current Density Imaging,” in *international society for magnetic resonance in medicine,* 2005, vol. 13, p. 2352.

[41] T. I. Oh, Y. Cho, Y. K. Hwang, S. H. Oh, E. J. Woo, and S. Y. Lee, “Improved Current Source Design to Measure Induced Magnetic Flux Density Distributions in MREIT,” *J. Biomed. Eng. Res.*, vol. 27, no. 1, pp. 30–37, 2006.

[42] Y. T. Kim, P. J. Yoo, T. I. Oh, and E. J. Woo, “Development of a low noise MREIT current source,” *J. Phys. Conf. Ser.*, vol. 224, no. 1, Apr. 2010.

[43] T. Topal, E. Değirmenci, R. Boyacıoğlu, V. E. Arpınar, and B. M. Eyüboğlu, “Current Source Design for MREIT Technique and Its Experimental Application,” in *15. Biyomedikal Mühendisliği Ulusal Toplantısı*, 2010, no. 3, pp. 3–6.

[44] Rıdvan Cantaş, “MODIFIED 3D SENSITIVITY MATRIX METHOD AND USE OF MULTICHANNEL CURRENT SOURCE FOR MAGNETIC RESONANCE ELECTRICAL IMPEDANCE TOMOGRAPHY,” Bilkent University, 2012.

[45] H. H. Eroğlu, B. M. Eyüboğlu, and C. Göksu, “Design and implementation of a bipolar current source for MREIT applications,” in *XIII Mediterranean Conference on Medical and Biological Engineering and Computing 2013 IFMBE Proceedings*, 2014, no. 2, pp. 161–164.

[46] E. Değirmenci, “High Resolution Imaging of Anisotropic Conductivity with Magnetic Resonance Electrical Impedance Tomography (MREIT),” METU, 2010.

[47] B. M. Eyüboğlu, “MAGNETIC RESONANCE — ELECTRICAL IMPEDANCE TOMOGRAPHY,” *WILEY - Encycl. Biomed. Eng. WILEY-Encyclopedia Biomed. Eng. (Metin Akay, ed.)*, vol. 4, pp. 2154–2162, 2006.

[48] Özbek Orçun, “Imaging Current Density Distribution Using 0.15T Magnetic Resonance Tomography,” METU, 2002.

[49] B. M. Eyüboğlu, R. Reddy, and J. S. Leigh, “Imaging electrical current density using nuclear magnetic resonance,” *ELEKTRİK*, vol. 6, no. 3, pp. 201–214, 1998.

[50] Z. Liang, “A Model-Based Method for Phase Unwrapping,” *IEEE Trans. Med. Imaging*, vol. 15, no. 6, pp. 893–897, 1996.

[51] J. S. Lim, *Two-dimensional Signal and Image Processing*. Upper Saddle River, New Jersey 07458: Prentice HALL PTR, Prentice Hall Inc., 1990, pp. 476–483.

[52] J. Strand and T. Taxt, “Performance evaluation of two-dimensional phase unwrapping algorithms,” *Appl. Opt.*, vol. 38, no. 20, pp. 4333–4344, 1999.

[53] F. S. Operation, *MC78XX / LM78XX / MC78XXA 3-Terminal 1A Positive Voltage Regulator*. 2001.

[54] Mikroelektronika, *User's Guide to Mikromedia Board for dsPIC33*. 2011.

[55] T. Instruments, *DAC0800, DAC0802 8-Bit Digital-to-Analog Converters*. 2006.

[56] I. Rectifier, *Series PVX6012 Microelectronic Power IC Relay*. 2003.

[57] L. Technology, *Application Note 19, LT1070 Design Manual*. 1986.

[58] N. Mohan, T. M. Undeland, and W. P. Robbins, *Power Electronics Convertors, Applictions, and Design*, 3rd ed. John Wiley & Sons, Inc., 2003, pp. 172–178.

[59] A. Martin, "Boost Converter Design Tips," no. March. National Semiconductor, pp. 1–45, 2005.

[60] S. S. Deswal, R. Dahiya, and D. K. Jain, "Application of Boost Converter for Ride-through Capability of Adjustable Speed Drives during Sag and Swell Conditions," *World Acad. Sci. Eng. Technol.*, vol. 47, pp. 282–286, 2008.

[61] H. H. Eroğlu and B. M. Eyüboğlu, "Design and Implementation of a Monopolar Constant Current Stimulator," in *BIYOMUT 2012 Conference Proc.*, 2012, pp. 1–4.

[62] I. Rectifier, "IR2110(-1-2)(S)PbF/IR2113(-1-2)(S)PbF HIGH AND LOW SIDE DRIVER." 2005.

[63] I. Rectifier, "Application Note AN-1100." .

[64] I. Rectifier, "Application Note AN-978." 2007.

[65] V. Siliconix, "IRF740, SiHF740, Power MOSFET." 2012.

[66] T. I. Burr-Brown Products, "OPA452 OPA453 80V, 50mA Operational Amplifiers Datasheet." 2000.

[67] A. Devices, *Circuit Note CN-0151, Versatile High Precision Programmable Current Sources Using DAC's, Op Amps, and MOSFET Transistors*. 2011.

[68] Avago Technologies, "HFBR-0508Z Series HFBR-1528Z Transmitter HFBR-2528Z Receiver 10 Megabaud Versatile Link Fiber Optic Transmitter and Receiver for 1mm POF and 200um HCS." 2011.

[69] F. S. Operation, "FOD060L, FOD260L, FOD063L LVTTL/LVCMOS 3.3V High Speed-10MBit/s Logic Gate Optocouplers." 2005.

[70] M. Sadighi, “Magnetic Resonance Current Tensor Imaging (MRCTI) in 3T MRI System,” METU, 2013.

[71] C. Gabriel, S. Gabriel, and E. Corthout, “The dielectric properties of biological tissues: I. Literature survey.,” *Phys. Med. Biol.*, vol. 41, no. 11, pp. 2231–49, Nov. 1996.